

A One-Step Blended Soundproof-Compressible Model with Balanced Data Assimilation: Theory and Idealized Tests

RAY CHEW,^a TOMMASO BENACCHIO,^b GOTTFRIED HASTERMANN,^a AND RUPERT KLEIN^a

^a *FB Mathematik und Informatik, Freie Universität Berlin, Berlin, Germany*

^b *MOX-Modelling and Scientific Computing, Dipartimento di Matematica, Politecnico di Milano, Milan, Italy*

(Manuscript received 8 July 2021, in final form 8 November 2021)

ABSTRACT: A challenge arising from the local Bayesian assimilation of data in an atmospheric flow simulation is the imbalances it may introduce. Acoustic fast-mode imbalances of the order of the slower dynamics can be negated by employing a blended numerical model with seamless access to the compressible and the soundproof pseudo-incompressible dynamics. Here, the blended modeling strategy by Benacchio et al. is upgraded in an advanced numerical framework and extended with a Bayesian local ensemble data assimilation method. Upon assimilation of data, the model configuration is switched to the pseudo-incompressible regime for one time step. After that, the model configuration is switched back to the compressible model for the duration of the assimilation window. The switching between model regimes is repeated for each subsequent assimilation window. An improved blending strategy for the numerical model ensures that a single time step in the pseudo-incompressible regime is sufficient to suppress imbalances coming from the initialization and data assimilation. This improvement is based on three innovations: (i) the association of pressure fields computed at different stages of the numerical integration with actual time levels, (ii) a conversion of pressure-related variables between the model regimes derived from low Mach number asymptotics, and (iii) a judicious selection of the pressure variables used in converting numerical model states when a switch of models occurs. Idealized two-dimensional traveling vortex and buoyancy-driven bubble convection experiments show that acoustic imbalances arising from data assimilation can be eliminated by using this blended model, thereby achieving balanced analysis fields.

SIGNIFICANCE STATEMENT: Weather forecasting models use a combination of physics-based algorithms and meteorological measurements. A problem with combining outputs from the model with measurements of the atmosphere is that insignificant signals may generate noise and compromise the physical soundness of weather-relevant processes. By selecting atmospheric processes through the toggling of parameters in a mixed model, we propose to suppress the undesirable signals in an efficient way and retain the physical features of solutions produced by the model. The approach is validated here for acoustic imbalances using a compressible/pseudo-incompressible model pair. This development has the potential to improve the techniques used to bring observations into models and with them the quality of atmospheric model output.

KEYWORDS: Atmosphere; Filtering techniques; Kalman filters; Numerical analysis/modeling; Anelastic models; Data assimilation; Ensembles; Idealized models; Nonhydrostatic models

1. Introduction


a. Motivation

Dynamical processes in the atmosphere evolve on a range of spatiotemporal scales, most comprehensively expressed by the full compressible flow equations. Limit regimes, derived from the full compressible flow equations by scale analysis and asymptotics, describe reduced dynamics, examples being the soundproof anelastic and pseudo-incompressible models traditionally used at small- to mesoscale, and the hydrostatic

primitive equations at large to planetary scales (Pedlosky 2013; Vallis 2017; Klein 2010).

To access the dynamics of the full compressible flow equations and of their limit regimes, separate numerical schemes can be developed for each of the limiting models. From a computational perspective, however, the discrepancies between numerical solutions of different equation sets obtained by essentially the same numerical scheme can be substantially smaller than the discrepancies associated with the solution of one and the same equation set by different numerical schemes (Smolarkiewicz and Dörnbrack 2008; Klein 2009).

Benacchio et al. (2014), Klein et al. (2014), and, separately, Smolarkiewicz et al. (2014) developed discretization schemes for the compressible equations that allow access to the pseudo-incompressible model within a single numerical framework,

 Denotes content that is immediately available upon publication as open access.

Benacchio's current affiliation: Leonardo S.p.A., Cascina Costa, Varese, Italy.

Corresponding author: Ray Chew, ray.chew@fu-berlin.de



This article is licensed under a [Creative Commons Attribution 4.0 license](http://creativecommons.org/licenses/by/4.0/) (<http://creativecommons.org/licenses/by/4.0/>).

DOI: 10.1175/MWR-D-21-0175.1

© 2022 American Meteorological Society. For information regarding reuse of this content and general copyright information, consult the [AMS Copyright Policy](https://www.ametsoc.org/PUBSReuseLicenses/) (www.ametsoc.org/PUBSReuseLicenses/).

showing equivalent results of both configurations in small- to mesoscale tests involving acoustically balanced flows. The blended analytical and numerical framework in Benacchio et al. (2014) and Klein et al. (2014), within which the compressible to pseudo-incompressible transition is realized as a continuum of models controlled by an appropriate *blending parameter*, was conceptually extended in Klein and Benacchio (2016) to include access to hydrostatic models. Benacchio and Klein (2019) then proposed a numerical implementation and achieved equivalence of hydrostatic and nonhydrostatic model solutions on large scales in the absence of vertically propagating acoustic modes.

Balanced data assimilation provides a key motivation for blended numerical models. A problem with local data assimilation is the imbalance that it may induce (Lorenc 2003). As the assimilation procedure does not take heed of specific characteristics of a flow, such as conservation of mass, momentum, and energy, or of particular smoothness properties, the initial balance of a flow state may be destroyed by the assimilation procedure, see Neef et al. (2006) and more specifically Greybush et al. (2011) and Bannister (2015) on the effects of localization on balanced analysis fields.

Physically, local data assimilation in a compressible framework can introduce imbalances through fast acoustic modes with velocity amplitudes that may be of the same order of magnitude as the velocities found in the slowly evolving balanced dynamics of interest, with potentially destructive effects on overall solution quality (Hohenegger and Schär 2007). Judicious use of a blended soundproof-compressible model can be employed to counteract this effect. Imbalances inherent in the initial pressure fields can be effectively reduced by solving the initial time steps of a simulation in the pseudo-incompressible regime so that, upon the subsequent transition to the compressible regime over several further time steps, the pressure field is balanced with respect to the initial velocities and potential temperature fields (Benacchio et al. 2014; Klein et al. 2014). More specifically, the algorithm leverages a discrete projection of the velocity field onto the space of pseudo-incompressible solutions that is orthogonal in a L^2 -inner product weighted by the mass-weighted potential temperature, up to numerical truncation errors. Additional measures guarantee that the pressure field, too, corresponds to the physically correct pseudo-incompressible pressure and not to the Lagrange multiplier calculated as part of the projection. Therefore, the scheme provides the ensemble of balanced solutions closest to the analysis ensemble with respect to the norm induced by the mentioned inner product.

By extension of this insight, when mounting data assimilation on the numerics, a projection of the solution onto the soundproof pseudo-incompressible model can suppress the fast acoustic modes arising from the assimilation procedure. After suppression of the fast modes, the remaining time steps until the next assimilation procedure are solved with the compressible model. As this method makes use of the different dynamics modeled by the compressible and soundproof equation sets, it fundamentally deviates from existing methods to handle initialization problems such as the post-analysis digital filter (DFI; e.g., Lynch and Huang 1992) and the incremental

analysis update (IAU; Bloom et al. 1996). These techniques act as low-pass filters, and repeated application of the filter may have undesirable effects on long-term dynamics (Houtekamer and Zhang 2016; Polavarapu et al. 2004).

Balance was also shown to improve with the choice of localization space (Kepert 2009) and by allowing observations outside of a localization radius to relax to a climatological mean (Flowerdew 2015). Hastermann et al. (2021) compared the effects of the blending approach with those of the postanalysis penalty method in achieving balanced analysis fields for highly oscillatory systems and found comparable improvements for both methods in the case of nonlinear balance relations. See also Zupanski (2009) and Houtekamer and Zhang (2016) for reviews of balanced atmospheric data assimilation.

b. Contributions

This paper proposes a dynamics-driven method to achieve balanced data assimilation using a blended numerical framework with the following advances:

- One-step blending of the pseudo-incompressible and compressible models by instantaneous switching. This is achieved by (i) accounting for the fact that Exner pressure fields computed at comparable stages within a time step correspond to different time levels in the compressible and soundproof model; (ii) judiciously converting the thermodynamic variables between the compressible and soundproof models motivated by low Mach number asymptotic arguments; and (iii) carefully selecting, based on steps (i) and (ii), the pressure variables used in converting numerical model states at the blending time interfaces. One-step blending is a sizeable improvement over Benacchio et al. (2014), who needed several intermediate time steps for the blending procedure.
- Exploitation of the blended framework for balanced ensemble data assimilation. We employ an untuned data assimilation scheme that is known to introduce imbalances. After each assimilation of data, a single time step in the pseudo-incompressible model configuration is used to suppress the fast acoustic imbalances. The model configuration is then switched back to the compressible model. In the reported idealized experiments, balanced analysis fields are obtained by combining data assimilation and blending, thus verifying the ability of the blended model to handle imbalances consistently with the underlying compressible and soundproof dynamics.

The effects of data assimilation and blending on balanced solutions are investigated in the two-dimensional numerical experiments of a traveling vortex and of a rising thermal in a vertical slice (see Kadioglu et al. 2008; Mendez-Nunez and Carroll 1994; Klein 2009). For these tests, unbalanced and untuned data assimilation is shown here to destroy solution quality, while the use of blending effectively recovers the structure of the solution as evaluated by comparison with runs without data assimilation. Moreover, with the balanced data assimilation procedure, the solution quality of the observed quantities is maintained or improved independently of the size of the localization region, which is an important tunable parameter of many sequential data assimilation

procedures. The order of magnitude of the imbalances introduced by data assimilation in these idealized test cases is quantified by scale analysis.

The paper is structured as follows. Section 2 contains a brief introduction to data assimilation and the Kalman filters considered here. Section 3 reviews the blended numerical framework. Section 4 proposes the new blending scheme and section 5 details the results of numerical experiments. The effectiveness of the one-step blended soundproof-compressible scheme is investigated for balanced data initialization in section 5a, and its application toward balanced data assimilation in section 5c. Section 6 contains a discussion and the conclusions.

2. Data assimilation: A quick primer

Data assimilation is used in numerical weather prediction to improve forecasting. Existing approaches include 4D-Var, which optimizes model states over a finite time horizon in the past before launching a new prediction, and sequential assimilation procedures, which assimilate the available observations at specific points in time. Here we focus on the latter, which are more susceptible to the problem of imbalances addressed in this paper due to the local nature of these methods and especially when the localization is severe (Cohn et al. 1998; Mitchell et al. 2002).

Modern weather forecasting techniques aim to represent the uncertainty of a forecast by generating an ensemble of likely candidates of model states. Such an ensemble can be understood as an approximate representation of a probability distribution over model states. The task of sequential data assimilation is then as follows. Suppose we are given the probabilistic weight of each ensemble member at a previous instance in time, i.e., at the beginning of the current simulation window, together with the forward simulation states of all ensemble members at the current time, i.e., at the end of the simulation window. Then the prior probability distribution $\text{pdf}_{\text{prior}}$ is represented by the model states at the new time level together with their probabilistic weights inherited from the beginning of the simulation window. Now we are to readjust the current states or the probabilistic weights of the ensemble members, at fixed time, such that the resulting posterior probability distribution pdf_{post} best reflects the observations that have arrived during the simulation window.

The connection between $\text{pdf}_{\text{prior}}$ and pdf_{post} can be established in a Bayesian framework. For this purpose we assume no model error and $\mathbf{x}_{\text{truth}}$ to be a perfectly resolved, true model state. We denote the observation operator by \mathcal{H} . Then, observations that have arrived during the simulation window are subject to Gaussian distributed noise ϵ and satisfy

$$\mathbf{y}_{\text{obs}} = \mathcal{H}(\mathbf{x}_{\text{truth}}) + \epsilon. \quad (1)$$

Now Bayes's theorem gives

$$\text{pdf}_{\text{post}}(\mathbf{x}) = \text{pdf}(\mathbf{x}|\mathbf{y}_{\text{obs}}) = \frac{\text{pdf}(\mathbf{y}_{\text{obs}}|\mathbf{x})}{\text{pdf}(\mathbf{y}_{\text{obs}})} \text{pdf}_{\text{prior}}(\mathbf{x}). \quad (2)$$

Here $\text{pdf}(\mathbf{x}|\mathbf{y}_{\text{obs}})$ is the conditional probability of state \mathbf{x} given the observations \mathbf{y}_{obs} and $\text{pdf}(\mathbf{y}_{\text{obs}}|\mathbf{x})$ is the probability of

observation \mathbf{y}_{obs} given the state \mathbf{x} . The right-hand side of Eq. (2) is computable given the information before the data assimilation step, noting that the best available estimate of $\text{pdf}(\mathbf{y}_{\text{obs}})$ is the expectation of $\text{pdf}(\mathbf{y}_{\text{obs}}|\mathbf{x})$ with respect to \mathbf{x} under the prior probability distribution. See Wikle and Berliner (2007) and Reich and Cotter (2013) for more details on Bayesian data assimilation.

The Kalman filters

Kalman filters are a family of popular Bayesian-based data assimilation methods (Kalman 1960) that assumes Gaussian shape for all probability densities so that they can be fully characterized by their means and covariance matrices. Identifying the prior with the term *forecast* (f), and the posterior with the term *analysis* (a), the Kalman filter is

$$\begin{aligned} \mathbf{x}^a &= \mathbf{x}^f + \mathbf{B}\mathcal{H}^T(\mathcal{H}\mathbf{B}\mathcal{H}^T + \mathbf{R})^{-1}[\mathbf{y}_{\text{obs}} - \mathcal{H}(\mathbf{x}^f)] \\ &= \mathbf{x}^f + \mathbf{K}[\mathbf{y}_{\text{obs}} - \mathcal{H}(\mathbf{x}^f)], \end{aligned} \quad (3)$$

where $\mathbf{B} \in \mathbb{R}^{m \times m}$ and $\mathbf{R} \in \mathbb{R}^{l \times l}$ are the covariance matrices associated with the forecast and observations, respectively. The m and l variables represent the dimension of the state and observation spaces. The term \mathbf{K} is the Kalman gain, which rewards the forecast if $\|\mathbf{B}\| \ll \|\mathbf{R}\|$ and penalizes it if $\|\mathbf{R}\| \ll \|\mathbf{B}\|$, where $\|\cdot\|$ is a suitable norm.

A class of Monte Carlo-based Kalman filters, the ensemble Kalman filters, avoid the problem of high dimensionality by approximating the underlying probability density functions through the empirical distributions given by an ensemble of individual simulation states (Reich and Cotter 2015). As a consequence, ensemble-based methods are often computationally more efficient than any scheme that aims to explicitly describe entire probability density functions.

Specifically, for an ensemble of size K , the ensemble forecast is $\{\mathbf{x}_1^f, \dots, \mathbf{x}_K^f\}$ and the ensemble's parametric information specifying its probability distribution is updated by

$$\bar{\mathbf{x}}^a = \bar{\mathbf{x}}^f + \mathbf{K}^{\text{ens}}[\mathbf{y}_{\text{obs}} - \mathcal{H}(\bar{\mathbf{x}}^f)], \quad (4a)$$

$$\mathbf{P}_K^a = \mathbf{P}_K^f - \mathbf{K}^{\text{ens}}\mathcal{H}\mathbf{P}_K^f, \quad (4b)$$

$$\mathbf{K}^{\text{ens}} = \mathbf{P}_K^f\mathcal{H}^T(\mathcal{H}\mathbf{P}_K^f\mathcal{H}^T + \mathbf{R})^{-1}, \quad (4c)$$

where $\bar{\mathbf{x}}^{\text{alf}}$ is the ensemble mean and $\mathbf{P}_K^{\text{alf}} \in \mathbb{R}^{K \times K}$ is the covariance associated with the ensemble.

A drawback to the ensemble Kalman filter is that the covariance is determined by the spread of the ensemble and is therefore typically underestimated. However, ensemble inflation can be applied by multiplying the ensemble covariance by a constant factor larger than 1. This increases the covariance in the direction of the ensemble spread (Anderson 2007; Van Leeuwen et al. 2015).

This paper uses the local ensemble transform Kalman filter (LETKF) data assimilation method (Hunt et al. 2007) based on the ensemble square root filter (ESRF). The LETKF localizes the observation covariance in such a way that observations farther away from the grid point under analysis have less

influence, tapering off to zero influence for observations outside of a prescribed observation radius. The algorithm for the LETKF is provided in [appendix A](#).

Localization prevents spurious correlations of faraway observations while potentially reducing the complexity of the problem by making the observation covariance matrix closer to diagonal ([Hamill et al. 2001](#); [Houtekamer and Mitchell 1998](#)). After localization, the analysis is only performed on a smaller local region, and the global analysis ensemble comprises different linear combinations of the ensemble members in each of these local regions. This allows the ensemble to represent a higher-dimensional space than one constrained by the ensemble size ([Fukumori 2002](#); [Mitchell et al. 2002](#)). A smaller ensemble size may necessitate more severe localization.

When applying the LETKF, there are two potential sources for imbalances. In the case of a nonlinear balance relation, the LETKF fails to recover the desired balance due to its local linear construction. Even without localization and for a given observation, the analysis ensemble of the ESRF is obtained as a linear combination of the forecast ensemble. In the case of linear balances, the situation is more subtle. On one hand the ESRF without localization is capable of resolving linear balances due to its linear construction. On the other hand the LETKF, utilizing localization, does not act as a linear map on the global fields and therefore does not necessarily preserve the balance relation. Numerical experiments in this paper investigate imbalances arising from both these sources.

A smooth localization function, such as the truncated Gaussian function or the [Gaspari and Cohn \(1999\)](#) function, may be used to keep the resulting fields sufficiently smooth.

3. The blended numerical model

a. Governing equations

In a rotating three-dimensional Cartesian domain, the adiabatic, dry compressible fluid flow equations for an ideal gas under gravity are as follows:

$$\rho_t + \nabla_{\parallel} \cdot (\rho \mathbf{u}) + (\rho w)_z = 0, \quad (5a)$$

$$(\rho \mathbf{u})_t + \nabla_{\parallel} \cdot (\rho \mathbf{u} \circ \mathbf{u}) + (\rho w \mathbf{u})_z = -[c_p P \nabla_{\parallel} \pi + f \mathbf{k} \times \rho \mathbf{u}], \quad (5b)$$

$$(\rho w)_t + \nabla_{\parallel} \cdot (\rho \mathbf{u} w) + (\rho w^2)_z = -(c_p P \pi_z + \rho g), \quad (5c)$$

$$\alpha_p P_t + \nabla_{\parallel} \cdot (P \mathbf{u}) + (P w)_z = 0, \quad (5d)$$

where ρ is the density, $\mathbf{u} = (u, v)$ is the vector of horizontal velocities, w is the vertical velocity, P is the mass-weighted potential temperature, and π is the Exner pressure. The variable f is the Coriolis parameter on the horizontal (x, y) plane, \mathbf{k} is a unit vector in the vertical direction, and \times represents the cross product. The term g is the acceleration of gravity acting in the direction of \mathbf{k} ; the \circ denotes the tensor product and ∇_{\parallel} denotes the horizontal gradient, while the subscripts t and z denote the partial derivatives with respect to time t and the vertical coordinate z .

The terms π and P are related to the thermodynamic pressure p by the equation of state:

$$\pi = \left(\frac{p}{p_{\text{ref}}} \right)^{R/c_p}, \quad P = \frac{p_{\text{ref}}}{R} \left(\frac{p}{p_{\text{ref}}} \right)^{c_p/c_p} = \rho \Theta, \quad (6)$$

where p_{ref} is a reference pressure; c_p and c_v are the heat capacities at constant pressure and constant volume, respectively; $R = c_p - c_v$ is the ideal gas constant; and Θ is the potential temperature. The parameter α_p tunes between the compressible and the pseudo-incompressible model ([Durran 1989](#); [Klein et al. 2010](#)).

Identifying χ with the inverse potential temperature:

$$\chi = \frac{1}{\Theta}, \quad (7)$$

the Exner pressure and inverse potential temperature can be decomposed as

$$\pi = \bar{\pi} + \pi', \quad \text{and} \quad (8a)$$

$$\chi = \bar{\chi} + \chi', \quad (8b)$$

where the bar denotes a hydrostatic background state, which depends only on the vertical coordinate, and the prime denotes the perturbation. Rewriting (5) with (7) yields

$$\rho_t + \nabla_{\parallel} \cdot (P \mathbf{u} \chi) + (P w \chi)_z = 0, \quad (9a)$$

$$(\rho \mathbf{u})_t + \nabla_{\parallel} \cdot (P \mathbf{u} \circ \chi \mathbf{u}) + (P w \chi \mathbf{u})_z = -[c_p P \nabla_{\parallel} \pi + f \mathbf{k} \times \rho \mathbf{u}], \quad (9b)$$

$$(\rho w)_t + \nabla_{\parallel} \cdot (P \mathbf{u} \chi w) + (P w \chi w)_z = -(c_p P \pi_z + \rho g), \quad (9c)$$

$$\alpha_p P_t + \nabla_{\parallel} \cdot (P \mathbf{u}) + (P w)_z = 0. \quad (9d)$$

Using the notation of [Smolarkiewicz et al. \(2014\)](#) and [Benacchio and Klein \(2019\)](#):

$$\Psi = (\chi, \chi \mathbf{u}, \chi w, \chi'), \quad (10)$$

Eq. (9) can be written compactly as

$$(P \Psi)_t + \mathcal{A}(\Psi; P \mathbf{v}) = Q(\Psi; P), \quad (11a)$$

$$\alpha_p P_t + \nabla \cdot (P \mathbf{v}) = 0, \quad (11b)$$

where $\mathbf{v} = (u, v, w)$ subsumes the three-dimensional velocity fields, $\mathcal{A}(\Psi; P \mathbf{v})$ denotes the advection of the quantity Ψ given the advective fluxes $P \mathbf{v}$, while $Q(\Psi; P)$ describes the effect on the right-hand side of (9) on Ψ given P .

From (6), P is a function of π only,

$$P(\pi) = \frac{p_{\text{ref}}}{R} \pi^{1/(\gamma-1)}, \quad (12)$$

where $\gamma = c_p/c_v$ is the isentropic exponent. With (12), (11b) becomes

$$\alpha_P \left(\frac{\partial P}{\partial \pi} \right) \pi'_t = -\nabla \cdot (P\mathbf{v}). \quad (13)$$

b. Summary of the numerical scheme

Equation (9d) is discretized in time with an implicit mid-point method:

$$\alpha_P P^{n+1} = \alpha_P P^n - \Delta t \nabla \cdot (P\mathbf{v})^{n+1/2}. \quad (14)$$

To obtain the advective fluxes at the half time level, the time-update for Eqs. (11a) and (11b) is split into advective and nonadvective terms. The advection terms on the left are updated by

$$(P\Psi)^\# = \mathcal{A}_{1st}^{\Delta t/2} [\Psi^n; (P\mathbf{v})^n], \quad (15a)$$

$$\alpha_P P^\# = \alpha_P P^n - \frac{\Delta t}{2} \tilde{\nabla} \cdot (P\mathbf{v})^n, \quad (15b)$$

where $\tilde{\nabla}$ is the discrete divergence and \mathcal{A}_{1st} is an advection scheme corresponding to the half time level update. The terms on the right are then advanced using an implicit Euler method:

$$(P\Psi)^{n+1/2} = (P\Psi)^\# + \frac{\Delta t}{2} Q(\Psi^{n+1/2}; P^{n+1/2}), \quad (16a)$$

$$\alpha_P P^{n+1/2} = \alpha_P P^n - \frac{\Delta t}{2} \tilde{\nabla} \cdot (P\mathbf{v})^{n+1/2}. \quad (16b)$$

Expressions (15) and (16) yield the advective fluxes at the half time level.

Subsequently, the quantities Ψ are updated to the full time level with an explicit Euler half step followed by a full advection step and a final implicit Euler half step:

$$(P\Psi)^* = (P\Psi)^n + \frac{\Delta t}{2} Q(\Psi^n; P^n), \quad (17a)$$

$$(P\Psi)^{**} = \mathcal{A}_{2nd}^{\Delta t} [\Psi^*; (P\mathbf{v})^{n+1/2}], \quad (17b)$$

$$(P\Psi)^{n+1} = (P\Psi)^{**} + \frac{\Delta t}{2} Q(\Psi^{n+1}; P^{n+1}), \quad (17c)$$

$$\alpha_P P^{n+1} = \alpha_P P^n - \Delta t \tilde{\nabla} \cdot (P\mathbf{v})^{n+1/2}, \quad (17d)$$

yielding a second-order accurate one-step method (Benacchio and Klein 2019; Smolarkiewicz 1991; Smolarkiewicz and Margolin 1993).

A first-order Runge–Kutta method is used for the advection operator $\mathcal{A}_{1st}^{\Delta t/2}$ in (15a) while second-order Strang splitting is used for $\mathcal{A}_{2nd}^{\Delta t}$ in (17b). The former is necessary for the time-level analysis in section 4 to hold and the latter guarantees second order in time of the overall scheme. The spatial discretization of the numerical scheme is based on a finite volume framework, for more details see section 4 in Benacchio and Klein (2019).

c. Pseudo-incompressible regime

The switch α_P in (5) toggles access to the pseudo-incompressible model ($\alpha_P = 0$, Durran 1989):

$$\rho_t + \nabla_{\parallel} \cdot (\rho\mathbf{v}) + (\rho w)_z = 0, \quad (18a)$$

$$(\rho\mathbf{u})_t + \nabla_{\parallel} \cdot (\rho\mathbf{u} \circ \mathbf{u}) + (\rho w\mathbf{u})_z = -[c_p P \nabla \pi + f\mathbf{k} \times \rho\mathbf{u}], \quad (18b)$$

$$(\rho w)_t + \nabla_{\parallel} \cdot (\rho w\mathbf{u}) + (\rho w^2)_z = -(c_p P \pi_z + \rho g), \quad (18c)$$

$$\nabla_{\parallel} \cdot (P\mathbf{u}) + (Pw)_z = 0, \quad (18d)$$

where (18d) enforces the soundproof divergence constraint. See Klein (2009), Klein and Pauluis (2012), and Klein and Benacchio (2016) for details of this formulation.

4. Single time-step soundproof-compressible transition

In the following, a conversion of pressure-related quantities, motivated by low Mach number asymptotics and applied prior to the model transitions, is proposed which allows for model switching within a single time step.

a. Time level of the pressure-related variables

In the simpler nonrotating case without gravity ($g, f = 0$), the update for the momentum equation multiplied by the potential temperature Θ in (16a) and (17c) read as

$$(P\mathbf{v})_t = -c_p (P\Theta)^{\text{adv}} \nabla \pi, \quad (19)$$

where the superscript “adv” denotes the quantity that becomes available after the advection substeps (15a) and (17b). Applying an implicit Euler discretization to (19), we find

$$(P\mathbf{v})^{\text{out}} = (P\mathbf{v})^{\text{in}} - \delta t c_p (P\Theta)^{\text{adv}} \tilde{\nabla} \pi^{\text{out}}, \quad (20)$$

where the superscript “in” denotes the quantities at the time level corresponding to the start of the time step and “out” at the end. The term $\delta t \leq \Delta t$ is an arbitrary time step size.

1) THE COMPRESSIBLE EQUATIONS

For the case $\alpha_P = 1$ and using (12), a discretization of the left-hand side of (13) yields at the half time level:

$$P^{n+1/2} - P^n = \left(\frac{\tilde{\partial} P}{\tilde{\partial} \pi} \right)^\# (\pi^{n+1/2} - \pi^n), \quad (21)$$

where $(\tilde{\partial} P / \tilde{\partial} \pi)^\#$ is obtained from P after the advection step at the half-time level, (15). Substituting (21) into (16b):

$$\left(\frac{\tilde{\partial} P}{\tilde{\partial} \pi} \right)^\# (\pi^{n+1/2} - \pi^n) = -\frac{\Delta t}{2} \tilde{\nabla} \cdot (P\mathbf{v})^{n+1/2}. \quad (22)$$

The right-hand side of (22) is obtained from the update in (20). In turn, $(P\mathbf{v})^{\text{in}}$ in (20) is the solution of the advection terms in (15):

$$(P\mathbf{v})^{\text{in}} = (P\mathbf{v})^n - \frac{\Delta t}{2} \tilde{\nabla} \cdot (P\mathbf{v} \circ \mathbf{v})^n, \quad (23)$$

with $\delta t = \Delta t/2$. Identifying out with $n + 1/2$ and rearranging, (22) becomes

$$\begin{aligned} & \left(\frac{\tilde{\partial} P}{\tilde{\partial} \pi} \right)^{\#} \pi^{n+1/2} - \left(\frac{\Delta t}{2} \right)^2 \tilde{\nabla} \cdot [c_p(P\Theta)^{\#} \tilde{\nabla} \pi^{n+1/2}] \\ & = \left(\frac{\tilde{\partial} P}{\tilde{\partial} \pi} \right)^{\#} \pi^n - \frac{\Delta t}{2} \tilde{\nabla} \cdot (P\mathbf{v})^n + \left(\frac{\Delta t}{2} \right)^2 \tilde{\nabla} \cdot [\tilde{\nabla} \cdot (P\mathbf{v} \circ \mathbf{v})^n], \end{aligned} \quad (24)$$

which fixes the time level of π after the half time-step of (15) and (16) at $n + 1/2$.

For the full-time stepping of (17), a similar procedure yields

$$\begin{aligned} & \left(\frac{\tilde{\partial} P}{\tilde{\partial} \pi} \right)^{\#} \pi^{n+1} - \left(\frac{\Delta t}{2} \right)^2 \tilde{\nabla} \cdot [c_p(P\Theta)^{\#} \tilde{\nabla} \pi^{n+1}] \\ & = \left(\frac{\tilde{\partial} P}{\tilde{\partial} \pi} \right)^{\#} \pi^n - \Delta t \tilde{\nabla} \cdot (P\mathbf{v})^n + \frac{(\Delta t)^2}{2} \tilde{\nabla} \cdot [\tilde{\nabla} \cdot (P\mathbf{v} \circ \mathbf{v})^{n+1/2}] \\ & \quad + \left(\frac{\Delta t}{2} \right)^2 \tilde{\nabla} \cdot [c_p(P\Theta)^{\#} \tilde{\nabla} \pi^n]. \end{aligned} \quad (25)$$

From (24), π is at time level $n + 1/2$ after the half-time stepping in (16) while (25) starts with π at time level n for the full-time stepping in (17). Therefore, the time level of π has to be reset from $n + 1/2$ to n after the half time-step in (16) and before the full time step in (17). Furthermore, the time level of π after the full time step in (17) is $n + 1$ as intended.

2) THE PSEUDO-INCOMPRESSIBLE EQUATIONS

For $\alpha_p = 0$, the coupling between P and π in (13) no longer holds and the two variables decouple, leading to

$$\nabla \cdot (P\mathbf{v}) = 0. \quad (26)$$

Enforcing this divergence constraint for the left-hand side of (20), we obtain

$$\tilde{\nabla} \cdot (P\mathbf{v})^{\text{in}} = \tilde{\nabla} \cdot [\delta t c_p(P\Theta)^{\text{adv}} \tilde{\nabla} \pi^{\text{out}}]. \quad (27)$$

At the half-time level, $(P\mathbf{v})^{\text{in}}$ is the solution of (15) comprising the half time-step advection. Therefore,

$$\tilde{\nabla} \cdot (P\mathbf{v})^{\text{in}} = \tilde{\nabla} \cdot \left[(P\mathbf{v})^n + \frac{\Delta t}{2} \tilde{\partial}_t (P\mathbf{v})^{\#} \right], \quad (28)$$

where $\tilde{\partial}_t$ is the discrete partial time derivative. As the second term is generated by (15) starting at time level n , i.e., by an explicit advection step associated with the left-hand side of (9b) and (9c) multiplied by Θ :

$$\tilde{\partial}_t (P\mathbf{v})^{\#} + \tilde{\nabla} \cdot (P\mathbf{v} \cdot \mathbf{v})^n = 0, \quad (29)$$

Eq (28) becomes

$$\tilde{\nabla} \cdot (P\mathbf{v})^{\text{in}} = \tilde{\nabla} \cdot (P\mathbf{v})^n - \frac{\Delta t}{2} \tilde{\nabla} \cdot [\tilde{\nabla} \cdot (P\mathbf{v} \circ \mathbf{v})^n]. \quad (30)$$

Inserting (30) back into (27), with $\delta t = \Delta t/2$:

$$\tilde{\nabla} \cdot \left[\frac{\Delta t}{2} c_p(P\Theta)^n \tilde{\nabla} \pi^n \right] = \tilde{\nabla} \cdot (P\mathbf{v})^n - \frac{\Delta t}{2} \tilde{\nabla} \cdot [\tilde{\nabla} \cdot (P\mathbf{v} \circ \mathbf{v})^n], \quad (31)$$

where the right-hand side has fixed the time level of π^{out} and adv at n . Equations (31) and (20) constitute a projection step that yields a divergence-free $(P\mathbf{v})^{n+1/2}$. The π^n solution in (31) is a compromise between controlling the divergence in $\tilde{\nabla} \cdot (P\mathbf{v})^n$ and making a time step of size $\Delta t/2$ to find a reasonable approximation of a pressure field obeying the nonlinear acoustic balance relation. Such a compromise may be avoided by introducing an additional projection step to recover a divergence-free $(P\mathbf{v})^{n*}$ before (31) is invoked on the basis of $(P\mathbf{v})^{n*}$. However, this is not done in practice, as the projection step outlined in Eqs. (31) and (20) is adequate in achieving balanced solutions for the idealized experiments in this paper.

For the full time stepping, $(P\mathbf{v})^{\text{in}}$ is the solution of (17b) and so (27) is

$$\tilde{\nabla} \cdot (P\mathbf{v})^{**} = \tilde{\nabla} \cdot \left[\frac{\Delta t}{2} c_p(P\Theta)^{**} \tilde{\nabla} \pi^{\text{out}} \right], \quad (32)$$

with

$$\tilde{\nabla} \cdot (P\mathbf{v})^{**} = \tilde{\nabla} \cdot \left[(P\mathbf{v})^n - \frac{\Delta t}{2} c_p(P\Theta)^n \tilde{\nabla} \pi^n + \Delta t \tilde{\partial}_t (P\mathbf{v})^{**} \right], \quad (33)$$

where the second term in the square brackets is a contribution from the explicit substep in (17a), and the third term is obtained as a result of the advection substep at the full time level.

Substitute (31) into (33):

$$\tilde{\nabla} \cdot (P\mathbf{v})^{**} = \tilde{\nabla} \cdot \left[\frac{\Delta t}{2} \tilde{\nabla} \cdot (P\mathbf{v} \circ \mathbf{v})^n + \Delta t \tilde{\partial}_t (P\mathbf{v})^{**} \right], \quad (34)$$

and note that advection substep (17b) solves the left-hand side of (9b) and (9c) multiplied with Θ :

$$\tilde{\partial}_t (P\mathbf{v})^{**} + \tilde{\nabla} \cdot (P\mathbf{v} \circ \mathbf{v})^{n+1/2} = 0, \quad (35)$$

where the half-time level of the second term emerges from the solution of substeps (17a) and (17b) under the advecting fluxes $(P\mathbf{v})^{n+1/2}$. Putting (34) and (35) together and inserting the result back into (32) gives

$$\tilde{\nabla} \cdot \left[c_p(P\Theta)^{**} \tilde{\nabla} \pi^{n+1} \right] = - \left(1 + \frac{\Delta t}{2} \tilde{\partial}_t \right) \tilde{\nabla} \cdot [\tilde{\nabla} \cdot (P\mathbf{v} \circ \mathbf{v})^{n+1/2}], \quad (36)$$

fixing the time level of π^{out} at $n + 1$, since the right-hand side is a half time-step advancement from the $n + 1/2$ time level.

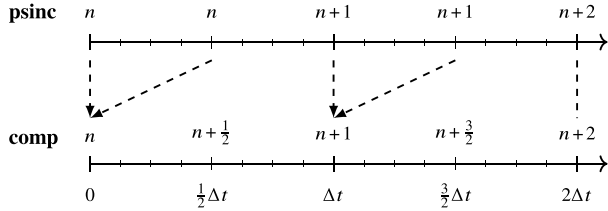


FIG. 1. Time levels of Exner pressure π in the pseudo-incompressible (psinc) and the compressible (comp) models. The dashed lines indicate that, from the time-level analysis, the π values are at the same physical time level between the two models. Arrows depict the two valid choices of π in the pseudo-incompressible to compressible blending at time t^n and t^{n+1} .

In contrast to the compressible case, expressions (31) and (36) imply that Exner pressure π after the half-step (15) and (16) is at the time level n , and could be used as the input to (17) as an alternative to using the Exner pressure obtained at the end of time step $n - 1$. Therefore, π may not have to be reset to time level n after the half-time predictor for the pseudo-incompressible solve. Figure 1 summarizes the time-level analysis of π .

b. Conversion of the pressure-related variables

Expression (8a) separates the background Exner pressure from its perturbation. For low Mach number flows, $\text{Ma} \ll 1$, such a separation is naturally induced by the asymptotic expansion:

$$\pi = \pi^{(0)} + \text{Ma}^2 \pi^{(1)} + \dots, \quad (37)$$

where $\text{Ma} = u_{\text{ref}}/c_{\text{ref}}$ for reference velocity u_{ref} and speed of sound c_{ref} . Substituting (37) into (13) yields

$$\alpha_p \left(\frac{\partial P}{\partial \pi} \right) \text{Ma}^2 \pi_t^{(1)} = -\nabla \cdot (P\mathbf{v}), \quad (38)$$

based on which we can blend the pseudo-incompressible ($\alpha_p = 0$) and compressible ($\alpha_p = 1$) models. Using (12), the mass-weighted potential temperature in the compressible model, P_{comp} , and its pseudo-incompressible counterpart, P_{psinc} , are related by

$$P_{\text{comp}} = (P_{\text{psinc}}^{\gamma-1} + \text{Ma}^2 \pi'_{\text{psinc}})^{1/(\gamma-1)}, \quad (39a)$$

$$P_{\text{psinc}} = (P_{\text{comp}}^{\gamma-1} - \text{Ma}^2 \pi'_{\text{comp}})^{1/(\gamma-1)}. \quad (39b)$$

Therefore, at the blending time interfaces between the compressible and the pseudo-incompressible configurations, one of the two expressions in (39) is applied depending on the direction of the transition.

c. Association of perturbation variables between the compressible and soundproof models

The time-level analysis of π in section 4a demonstrated that, in a pseudo-incompressible solve, both the Exner pressure solution after the full time step from t^n to t^{n+1} and that

obtained after the *subsequent* half time-step are associated with the same time level t^{n+1} .

Consider then the compressible to pseudo-incompressible transition at time $n + 1$. The term P_{psinc}^{n+1} is obtained by inserting π'_{comp}^{n+1} into the right-hand side of (39b). On the other hand, there are two valid choices for π' in a pseudo-incompressible to compressible transition [Fig. 1 and (39a)]: 1) π'_{full} , i.e., π' obtained after the full n to $n + 1$ time step; or 2) π'_{half} , i.e., π' obtained after the $n + 1$ to $n + 3/2$ half time-step.

The π'_{half} is obtained from the solution of (16) with the solution of (15) as its input. The input to (15) are Ψ^n and $(P\mathbf{v})^n$. This means that π'_{half} is recovered from the other quantities and is independent of π at the previous time level, so errors in the initialization of π are not propagated. By contrast, π'_{full} is obtained from the solution of (17). The explicit (17a) has π as an input to the right-hand side $Q(\Psi^n; P^n)$. Therefore, π'_{full} propagates errors in the initialization of π . Note that choice 2 entails solving an additional time step in the pseudo-incompressible regime to obtain π'_{half} at the pseudo-incompressible to compressible blending time interfaces.

In addition, choice 2 offers a conceptual advantage. The Exner pressure field in the pseudo-incompressible model is not controlled by an evolution equation but rather acts as a Lagrangian multiplier ensuring compliance of the velocity field with the divergence constraint at some fixed time. Thus, a direct dependence of the pressure on its previous time level data, as occurs under option 1), is a numerical artifact that should be avoided.

d. Data assimilation and blending

A data assimilation engine is used to insert observations in the fully compressible configuration of the blended numerical framework. Prior to the assimilation procedure at time t^n , the forecast ensemble state vector $\{\mathbf{x}_k^f\}^n$ for $k = 1, \dots, K$ and a set of observations $\mathbf{y}_{\text{obs}}^n$ are available. Here, K is the ensemble size. For vertical slice simulations with the full compressible flow equations, the ensemble state vector is

$$\{\mathbf{x}_1^f, \dots, \mathbf{x}_K^f\}^n = \{\rho, \rho u, \rho w, P, \pi'\}_{k=1, \dots, K}^n \in \mathbb{R}^{m \times K}. \quad (40)$$

Here, the two-dimensional spatial grid has $(N_x \times N_z)$ cells and $m = (5 \times N_x \times N_z)$. The observations of the momentum fields are

$$\mathbf{y}_{\text{obs}}^n = \{(\rho u)_{\text{obs}}, (\rho w)_{\text{obs}}\}^n \in \mathbb{R}^l, \quad (41)$$

where the subscript “obs” indicates that the data are obtained externally and are noisy and sparse, and $l = [2 \times N_{\text{obs}}(n)]$, with $N_{\text{obs}}(n)$ the time-dependent dimension of the sparse observation space. The observation covariance \mathbf{R}^n is determined by the observation noise.

The forward observation operator \mathcal{H} selects for each $\{\mathbf{x}_k^f\}^n$ in (40) the momenta $(\rho u)^n$ and $(\rho w)^n$ on the grid points corresponding to the sparse observations, thereby projecting $\mathbf{x}_k^{f,n}$ from the state space \mathbb{R}^m into observation space \mathbb{R}^l :

$$\mathbf{y}_k^{f,n} = \mathcal{H}(\mathbf{x}_k^{f,n}) \in \mathbb{R}^l, \quad k = 1, \dots, K. \quad (42)$$

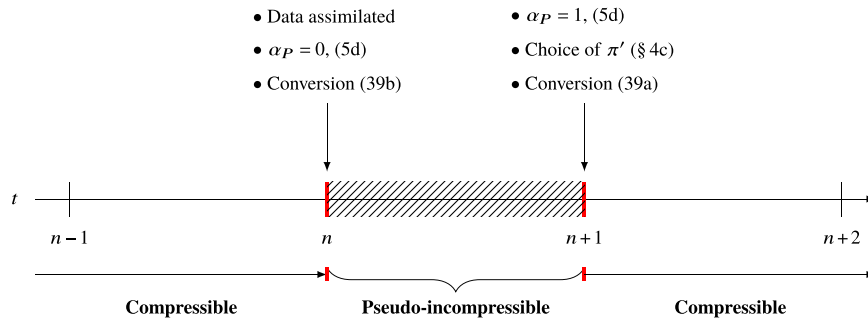


FIG. 2. Schematic of data assimilation with blending for data assimilated at time t^n . Blending time interfaces are in red, and the time step spent in the pseudo-incompressible regime is shaded. See main text for full description. Numbers in parentheses refer to equations, and (§) denotes the section.

The ensemble mean in observation space is computed as

$$\bar{\mathbf{y}}^{f,n} = \frac{1}{K} \sum_{k=1}^K \mathbf{y}_k^{f,n} \in \mathbb{R}^l. \quad (43)$$

A similar ensemble averaging is applied to obtain $\bar{\mathbf{x}}^{f,n}$. As observation localization is used in the LETKF algorithm (Hunt et al. 2007), only observations in a local region surrounding a given grid point are involved in its update. A localization function is furthermore applied to the observations in the local region (see section 5b and Table 2 for more details on the setup).

A Kalman gain \mathbf{K}^n similar to (4c) is obtained from the observation operator \mathcal{H} , the observation covariance \mathbf{R}^n , and an ensemble inflation factor b . As in the right-hand side of (4a), the distance of the forecast ensemble mean from the observations is computed with (41) and (43). From these, a set of K weight vectors $\{\mathbf{w}_k^n\}$ is obtained, applied to (40), and added to $\bar{\mathbf{x}}^{f,n}$, updating the forecast ensemble to the analysis ensemble. Further details are given in appendix A.

Once the assimilation procedure is completed, the model switches to the pseudo-incompressible limit regime and then back again to fully compressible until the next assimilation time. The process of switching back and forth between the model configurations exploits the blended numerical model to achieve balanced data assimilation and is termed blended data assimilation.

In particular, if data are assimilated into the compressible flow equations at time n , then compressible to pseudo-incompressible blending entails setting the switch α_P to 0 and converting the quantity P_{comp} with (39b). The solution is then propagated in the pseudo-incompressible regime for a time step, after which α_P is set back to 1, switching to the compressible flow equations. The quantity P_{psinc} is reconverted by (39a) using either π'_{half} or π'_{full} . Figure 2 summarizes the procedure. Following the analysis from section 4a, the perturbation variable π' is reset after the half time-stepping in the solution of the full model, but not in the solution of the limit model. The blended data assimilation workflow is displayed in Fig. 3.

As our principal strategy is to split measures of balancing the flow state from those of assimilating the data, we have not

tuned the data assimilation procedures themselves in any way. Tuning the data assimilation parameters may further improve balance, but as our balancing strategy is rather successful without tuning, the degrees of freedom of parameter tuning might be used more efficiently to achieve additional goals aside from the elimination of unphysical acoustic noise.

5. Numerical results

The idealized test cases of a traveling vortex and a rising warm air bubble are used to validate model performance in this section. To evaluate the effectiveness of the single time-step-blended soundproof-compressible scheme, unbalanced states are initialized in the compressible flow equations for both test cases and the blended scheme is applied. The balance of the compressible solution with unbalanced initial states is evaluated by “probe measurements,” i.e., by time series of the flow variables at selected points in the domain, and compared against analogous data extracted from the soundproof solution (Benacchio et al. 2014).

For blended ensemble data assimilation, an ensemble is generated by perturbing the initial conditions. Then, the blended scheme is applied after the assimilation of observations into the compressible flow equations and repeated after each assimilation procedure. The quality of balanced data assimilation is evaluated by root-mean-square errors with respect to a reference solution.

a. Effectiveness of the improved blending strategy

1) THE TRAVELING VORTEX EXPERIMENT

A stable configuration of the traveling vortex test case of Kadioglu et al. (2008) with $f = 0.0 \text{ s}^{-1}$ and $g = 0.0 \text{ m s}^{-2}$ is considered in the domain $x = [-5.0, 5.0] \text{ km}$, $z = [-5.0, 5.0] \text{ km}$ with doubly periodic boundary conditions and a background wind with velocity 100 m s^{-1} in both directions (Fig. 4). Changes made to the initial setup in Kadioglu et al. (2008) are given in appendix B. The time-step size is constrained by advective CFL = $\|\mathbf{u}\| \Delta t / \Delta x = 0.45$ on a (64×64) grid. This grid resolution is maintained for all traveling vortex experiments in this paper. The choice of reference units yields $\text{Ma} \approx 0.341$.

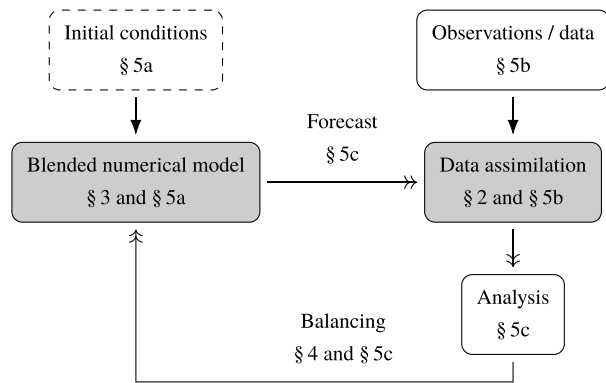


FIG. 3. Blended data assimilation workflow with the sections (§) of this paper describing the algorithmic components. The initial condition (dashed outline) is used only once to start the simulation. For each assimilation window, externally obtained observations/data are assimilated into the forecast and the algorithm loops through the components following the direction of the two-headed arrows.

Note, however, that while the background wind Mach number is relatively large, the superimposed vortex has a maximum flow velocity of 25 m s^{-1} with $\text{Ma}_{\text{vort}} = 0.085$, so that the low Mach number analysis of section 4b is justified.

To gauge the performance of the improved blended model, probe measurements of the full pressure increments δp are taken, defined, e.g., at time level n , as

$$\delta p^n = p^{n+1} - p^n. \quad (44)$$

at the center (0.0 km, 0.0 km). The first increment δp^0 corresponds to a spinup adjustment and is therefore omitted in the plots, as done in Benacchio et al. (2014).

The distance in the pressure increment result of a given run compared to the reference pseudo-incompressible run is quantified by the relative error E_ν ,

$$E_\nu = \frac{\|\delta p_\nu - \delta p_{\text{psinc}}\|_2}{\|\delta p_{\text{psinc}}\|_2}, \quad (45)$$

where $\nu = b$ for the blended run and $\nu = c$ for the imbalanced compressible run; $\|\cdot\|_2$ is the 2-norm taken over the probe measured time series of δp .

An imbalanced initial state is created by setting $P = 347.95 \text{ kg m}^{-2} \text{ K}$ and $\pi = 1.0$ over the whole domain for the full compressible flow equations (5) with $\alpha_p = 1$. For runs with blending, this imbalanced initial state is propagated for one time step in the limit pseudo-incompressible regime followed by the rest of the time steps in the fully compressible model. The blending scheme in section 4 is used to transition between the model regimes.

For this imbalanced initial state, a compressible run with blending is compared with a compressible run without blending and with a pseudo-incompressible run (left panel in Fig. 5). Fast acoustic modes are filtered from the blended solution and the result is indistinguishable from the limit

pseudo-incompressible reference solution, save for an initial adjustment in the first time step. Blending is able to recover the dynamics of the balanced state.

A close-up (right panel of Fig. 5) compares the blended runs with choices of π'_{half} and π'_{full} from section 4c against a run with the balanced initial state obtained from the known exact compressible vortex solution. The blended runs are as good as, and the π'_{half} run slightly closer to, the balanced compressible run. The relative error of the blended run with respect to the reference balanced run is 0.0319 using π'_{half} and 0.0381 using π'_{full} , corroborating the insight from section 4c that π'_{half} is a better choice. The choice of π'_{half} is used from here on for all experiments.

2) THE RISING BUBBLE EXPERIMENT

The second test consists of a gravity-driven thermal flow with $f = 0.0 \text{ s}^{-1}$ initialized as a bubble-shaped positive potential temperature perturbation $\delta\Theta$, on a constant isentropic background with $\Theta_0 = 300 \text{ K}$ in a $[-10.0, 10.0] \text{ km} \times [0.0, 10.0] \text{ km}$ domain, with periodic boundaries in x and no flux in z (Mendez-Nunez and Carroll 1994; Klein 2009; Benacchio et al. 2014). The dimensionless perturbation $\delta\Theta$ is defined by

$$\delta\Theta = \frac{2 \text{ K}}{\Theta_0} \cos\left(\frac{\pi}{2} r\right), \quad (46)$$

where

$$r = \frac{1}{r_0} \sqrt{x^2 + (z - z_0)^2}, \quad (47)$$

$r_0 = 2.0 \text{ km}$ is the initial radius of the bubble, and $z_0 = 2.0 \text{ km}$ the initial vertical displacement of the bubble.

The choice of reference units yields $\text{Ma} \approx 0.0341$. All rising bubble experiments presented in this paper are run on a grid with (160×80) cells to a final simulation time of 1000.0 s.

The initial pressure fields are set to reflect a horizontally homogeneous hydrostatic pressure field $\bar{p}(z)$ based on Θ_0 and initial condition $\bar{p}(0) = 86.1 \text{ kPa}$, with $\pi' \equiv 0.0$ [see (8a)]. These pressure data are imbalanced, however, with respect to the perturbed initial potential temperature $\Theta_0 + \delta\Theta$, see (46). Potential temperature at the initial and final time are depicted in Fig. 6.

The initial stages of the bubble evolution are compared for the compressible, pseudo-incompressible and one-step blended runs in Fig. 7. As the initial state is not hydrostatically balanced, pressure waves propagate in the compressible configuration (top-left panel) as seen in a time series of pressure perturbation increment probe measurements $\delta p'$ at $(x, z) = (-7.5, 5) \text{ km}$ (orange cross in the top-left panel and blue line in the top-right panel). Here, $p' = p - \bar{p}$. The acoustics are absent in the soundproof configuration (top-right panel, black line) and in the single time-step blended soundproof-compressible configuration (orange dots).

Next, the blended run and the pseudo-incompressible run are compared in more detail (Fig. 7, middle and bottom panels) with $\delta p'$. The probes are located at $(x, z) = (-7.5, 5) \text{ km}$ (middle panels) and at $(x, z) = (0, 5) \text{ km}$ (red cross in the

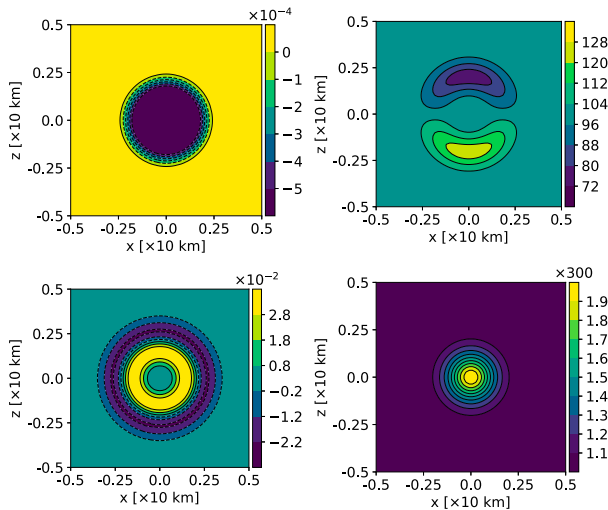


FIG. 4. Traveling vortex initial balanced states on a (64×64) grid: (top left) Exner pressure perturbation π' , dimensionless contours in the range $[-5, 0] \times 10^{-4}$ with interval of 10^{-4} ; (top right) horizontal velocity u , contours in the range $[72, 128] \text{ m s}^{-1}$ with a 8 m s^{-1} interval; (bottom left) vorticity, contours in the range $[-2.2, 2.8] \times 10^{-2} \text{ s}^{-1}$ with a $1.0 \times 10^{-2} \text{ s}^{-1}$ interval; and (bottom right) potential temperature θ , contours in the range $[1.1, 1.9] \times 300 \text{ K}$ with a $0.1 \times 300 \text{ K}$ interval. Negative contours are dashed.

top-left panel and bottom panels in Fig. 7), both with a constant small time step $\Delta t = 1.9 \text{ s}$ (top, middle-left, and bottom-left panels) and for larger, advective CFL-constrained time steps (middle-right and bottom-right panels, $\text{CFL} = 0.5$ and $\Delta t = 21.69 \text{ s}$ for the first two time steps). Away from the bubble trajectory (middle panels), the pressure perturbation increment due to the rising bubble and the remnants of the background acoustics from blending are comparable in amplitude. Larger amplitudes are observed with the blended model and the larger time step (middle-right panel), but they are still very small compared to the fully compressible run (note the different range on the vertical axes between the top-right and middle-right panels). On the bubble trajectory (bottom panels), the pressure perturbation increment due to the rising bubble dominates and the solutions are almost identical.

Throughout the runs, a single time step spent in the soundproof pseudo-incompressible regime largely filters out the fast acoustic imbalances of the compressible run (not shown in the middle and bottom panels of Fig. 7). This is quantified by comparing the relative errors with respect to the reference pseudo-incompressible run for the compressible run E_c and for the blended run E_b , defined in (45) and shown in Table 1. The blended run E_b is more than 25 times smaller than E_c for the large time-step case, and more than two orders of magnitude smaller for the small time-step case.

We also remark that a probe measurement of the full pressure time increment δp differs slightly between the reference pseudo-incompressible run and the one-step blended run (not shown). The difference is due to the time-dependence of the hydrostatically balanced background pressure \bar{p} in the blended run.

However, the computed values of the pressure perturbation time increment $\delta p'$ are remarkably similar in the two runs (black line and orange dots in top right panel of Fig. 7). We can thus conclude that blending recovers balanced dynamics irrespective of small compressibility-induced variations of the background pressure \bar{p} .

In view of these results, blending can be employed as an effective means to achieve the balanced initialization of data within a fully compressible model. The single time-step balancing capability in the model presented here substantially improves on the performance of Klein et al. (2014) and Benacchio et al. (2014), whose blended models achieved smaller reductions in amplitude compared to the fully compressible case and needed several time steps in the limit regime.

b. Ensemble data assimilation and blending: Setup

1) TRAVELING VORTEX SETUP

To combine blending with data assimilation as described in section 4d, an ensemble is generated by perturbing the initial vortex center position (x_c, z_c) within the open half interval of $[-1.0, 1.0 \text{ km}]$ for both x_c and z_c . The vortex is then generated around this center position such that the full vortex structure is translated. A total of 10 such samples are drawn, and they constitute the ensemble members. An additional sample is drawn and solved with the full model for the balanced initial condition. This run, denoted by obs, is used to generate the artificial observations. Another run with an identical setup to this additional obs sample is made. This time, however, blending for the first time step is applied and this run is considered the truth in the sequel. This is to correct for any errors in the initialization of π , as discussed in section 4c.

The choice of generating the truth and obs through a perturbation of the initial condition is such that the ensemble mean does not coincide with the truth. Otherwise, ensemble deflation alone would be sufficient to make the ensemble converge toward the truth, see also Lang et al. (2017).

The observations are taken from the obs run every 25 s—only a tenth of the grid points are observed and these are drawn randomly. Sparse observation grid points are randomly drawn as follows: A Boolean mask selecting for a tenth of the grid points is generated where if necessary, a ceiling function is applied to obtain an integer number of grid points selected. The entries of the mask are then shuffled using the algorithm by Fisher and Yates (1953), and the Boolean mask is applied to the obs array to obtain the sparse observations. This framework deviates from a more realistic situation where observations and grid points do not coincide. To simulate measurement noise, Gaussian noise with zero mean is added independently to each of the observed grid points. (The variances used in the experiments are listed in Table D1 and details on how the variances are computed are given in appendix D.) A similar method of generating artificial observations by adding independent Gaussian noise was used in, for example, Bocquet (2011) and Harlim and Hunt (2005) for the Lorenz-63 and Lorenz-96 models.

The regions for localized data assimilation are of size (11×11) grid points and only observations within such a patch are considered for analysis operations at the respective central grid

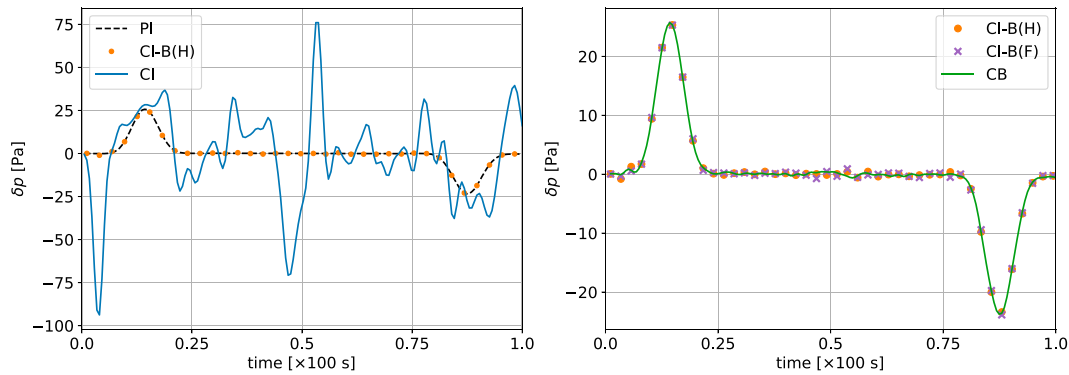


FIG. 5. Traveling vortex: Effect of one-step blending for imbalanced initial states on the time series of temporal increments of the full pressure δp at location $(x, z) = (0 \text{ km}, 0 \text{ km})$. (left) Comparison between a blended run using π'_{half} [orange dots; CI-B(H)], a run without blending (blue solid line; CI), and the reference solution from the pseudo-incompressible model (black dashed line; PI). (right) Comparison of blended runs using π'_{half} [orange dots; CI-B(H)] and π'_{full} [purple crosses; CI-B(F)], and the compressible solution with balanced initial states (green solid line; CB).

point. A localization function corresponding to a truncated Gaussian function is applied such that observations farther from the grid point under analysis have less influence, and that the influence decays smoothly toward the edges of the localization subdomain, where it is abruptly truncated to zero. No ensemble inflation is applied in this case.

Examples of the observations and truths used in the generation and evaluation of the experiments with data assimilation are displayed in Fig. 8. Notice that we run one test with observations of the momentum fields only, and another test with observations of the full set of variables.

The 10 ensemble members in each of these tests are initialized with balanced states, and blending is applied for the first

time step when the model runs in the pseudo-incompressible configuration. The ensemble is then solved forward in time with the fully compressible model. Data from the generated observations are assimilated every 25 s. The immediate time step after the assimilation procedure is solved in the pseudo-incompressible limit regime while the rest of the time steps in the assimilation window are solved using the full compressible model. Conversions according to the blending scheme in section 4 are employed when switching back and forth between the full and limit models. Furthermore, the choice of π'_{half} is used (cf. the discussion in section 4c.). The ensemble solved with both data assimilation and blending is abbreviated as EnDAB.

The setup is repeated for two additional ensembles and each observation scenario, one where data are still assimilated but no blending is performed (EnDA), and another where neither data assimilation nor blending are performed (EnNoDA). EnNoDA and EnDA constitute an identical twin experiment (Reich and Cotter 2015; Lang et al. 2017), through which the effects of data assimilation can be evaluated. EnDA along with EnDAB constitute yet another identical twin experiment, which evaluates the performance of blending.

2) RISING BUBBLE SETUP

The rising bubble ensemble spread is generated by randomly modifying the maximum of the potential temperature perturbation $\delta\theta$ in the open half interval $[2.0, 12.0 \text{ K})$. The ensemble comprises 10 members. While the relative spread of the temperature perturbation is large with this setup, the ensemble spread of the bubble position at the final time of the simulation, $t_{\text{fin}} = 1000.0 \text{ s}$, is only moderate.

An additional sample is drawn for the obs and the truth, which are identical in this setup. Blending is applied to the first time step of the obs and the truth, obtaining a balanced solution. As the rising bubble flow fields evolve rather slowly in the

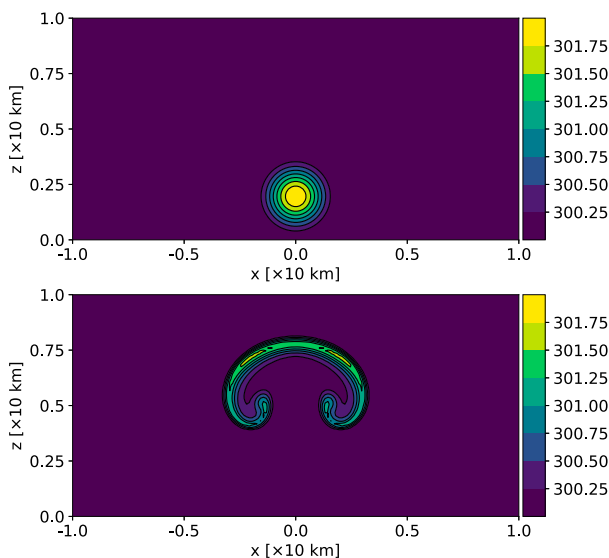


FIG. 6. Rising bubble on a (160×80) grid: Potential temperature at (top) initial time, $t = 0 \text{ s}$ and (bottom) final time $t_{\text{fin}} = 1000 \text{ s}$; contours in the range $[300.25, 301.75] \text{ K}$ with a 0.25-K interval.

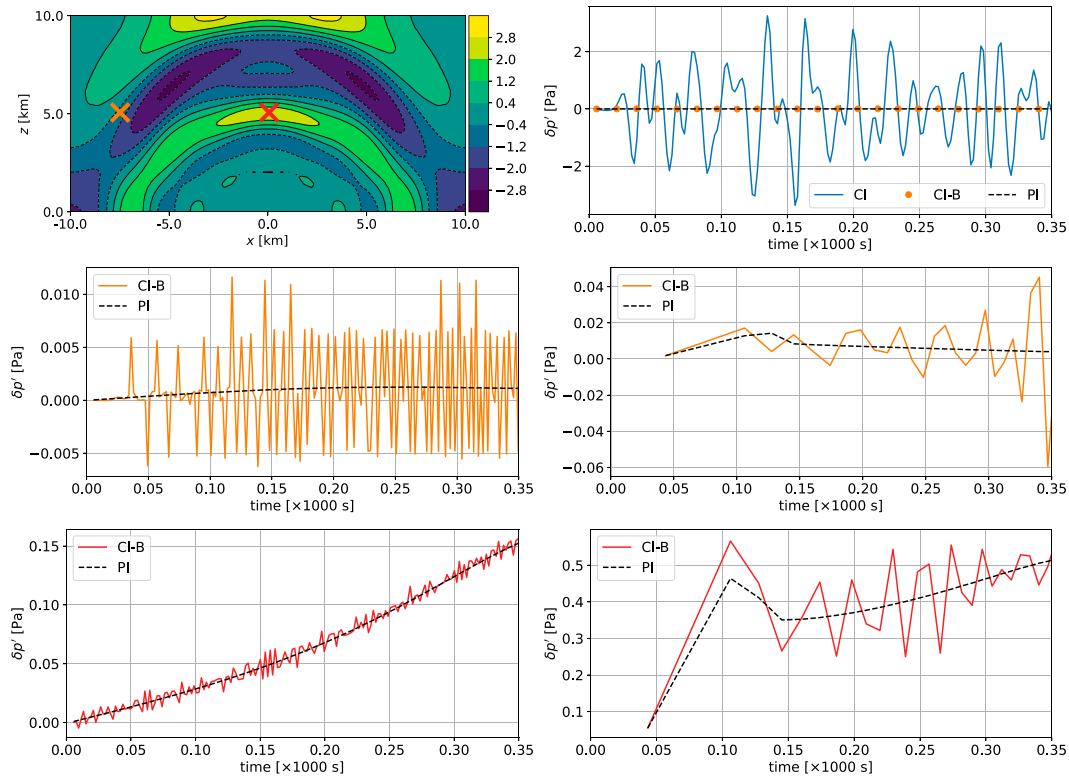


FIG. 7. Time increments $\delta p'$ of pressure perturbation in the rising bubble experiment. (top left) $\delta p'$ value at time step 14 ($t = 26.6$ s) for the compressible model with $\Delta t_{AC} = 1.9$ s; contours in the range $[-2.8, 2.8]$ Pa with an interval of 0.8 Pa, negative contours dashed. The orange cross marks $(x, z) = (-7.5, 5)$ km and the red cross $(x, z) = (0, 5)$ km. (top right) History of $\delta p'$ over the first 350 s measured at $(x, z) = (-7.5, 5)$ km for the compressible model (blue solid line; CI), the pseudo-incompressible model (black dashed line; PI) and the blended model with one pseudo-incompressible time step (orange dots; CI-B). History of $\delta p'$ over the first 350 s measured at (middle row) $(x, z) = (-7.5, 5)$ km and at (bottom row) $(x, z) = (0, 5)$ km. Pseudo-incompressible solution (black dashed line, PI) and blended solution with one time step spent in the pseudo-incompressible regime (CI-B; orange or red corresponding to the probe marker in the top-left panel). The top, middle-left, and bottom-left panels use a constant time step $\Delta t = 1.9$ s. The middle-right and bottom-right panels use $\Delta t = 21.69$ s for the first two time steps and then a Δt determined by advective CFL = 0.5.

beginning, data are only assimilated from $t = 500.0$ s onward. Observations of the momentum field are then assimilated every 50.0 s. As with the vortex experiments, only a tenth of the grid points are observed, independent Gaussian noise is added, and localization within an (11×11) grid points

TABLE 1. Errors E_c and E_b (see text for definitions) of the time series of $\delta p'$ in $[0, 1000]$ s relative to the reference pseudo-incompressible run (middle and bottom panels of Fig. 7). The acoustic time step size is $\Delta t_{AC} = 1.9$ s, while Δt_{ADV} is determined by advective CFL = 0.5 and $\Delta t_{ADV} = 21.69$ s for the first two time steps. Probe location $(-7.5, 5)$ km corresponds to the orange marker and orange lines in Fig. 7, and probe location $(0, 5)$ km corresponds to the red marker and red lines.

Probe location	Δt	E_c	E_b	E_c/E_b
$(-7.5, 5)$ km	Δt_{AC}	413.1822	1.4820	278.80
	Δt_{ADV}	109.7538	3.9034	28.12
$(0, 5)$ km	Δt_{AC}	10.1804	0.0311	327.34
	Δt_{ADV}	2.8231	0.1016	27.79

region is applied. (The variances used to generate the Gaussian noise are given in Table D1.) A localization function corresponding to the truncated Gaussian function is applied and the ensemble is not inflated. Examples of the observation and truth are given in Fig. 9. Three ensembles corresponding to the EnNoDA, EnDA, and EnDAB settings, with 10 members each, are generated, but only one set of experiments involving assimilation of the momentum field only is pursued.

Note that as the ensembles and the observations are generated with balanced initial conditions, any noise present in the simulation results is introduced by the data assimilation procedure. Table 2 summarizes the details of the data assimilation-related experimental setup for both test cases.

3) EVALUATION OF DATA ASSIMILATION

The quality of data assimilation is evaluated by a spatially and ensemble averaged root-mean-square error (RMSE) from the truth. The RMSE is given by

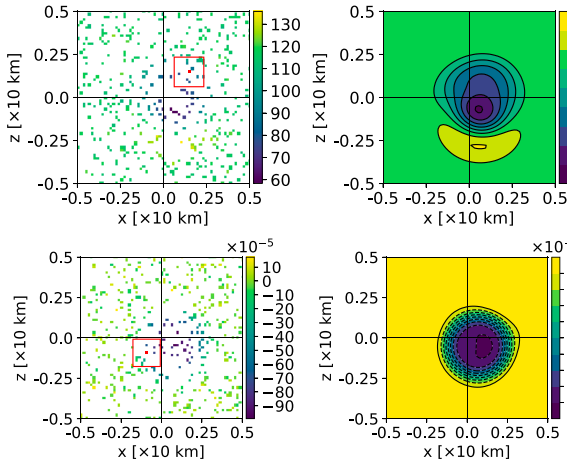


FIG. 8. Traveling vortex: (left) Sparse noisy observations and (right) truths at $t = 300.0$ s. (top) Horizontal momentum ρu , for the right panel, contours in the range $[60, 130] \text{ kg m}^{-1} \text{ s}^{-1}$ with a $10 \text{ kg m}^{-1} \text{ s}^{-1}$ interval. (bottom) Exner pressure perturbation π' ; for the right panel, dimensionless contours in the range $[-80, 0] \times 10^{-5}$ with an interval of 10^{-4} . Negative contours are dashed. The red squares illustrate, for an example grid point (in red), the observations considered in the local (11×11) gridpoint region.

$$\text{RMSE}(\psi) = \sqrt{\frac{1}{K} \frac{1}{N_x \times N_z} \sum_k^K \sum_{i,j}^{N_x, N_z} [\psi_k^{\text{ens}}(x_i, z_j) - \psi^{\text{truth}}(x_i, z_j)]^2}, \tag{48}$$

where $k = 1, \dots, K$ indexes the ensemble members and $i = 1, \dots, N_x$ and $j = 1, \dots, N_z$ the number of grid points in the (x, z) coordinates. The ψ is the set of quantities $\{\rho, \rho u, \rho w, P, \pi'\}$.

c. Ensemble data assimilation and blending: Results

1) TRAVELING VORTEX

Figure 10 depicts the ensemble snapshots for the vortex case with all quantities observed and assimilated. EnNoDA acts as the control ensemble, and the top row depicts its solutions for the traveling vortex without data assimilation and blending. While the center position of the vortex for each ensemble member is perturbed, the ensemble mean vortex position (right column) is centered around the origin. This is in line with the conditions used to generate the initial ensemble. With data assimilation, EnDA (middle row), the balance is lost and the vortex structure is not preserved at the final time. Data assimilation and blending, EnDAB (bottom row), recovers the balanced solution and the vortex structure is preserved after three periods of revolution. Moreover, comparing with Fig. 8, the effect of data assimilation becomes obvious. The center position of the EnDAB ensemble mean is in the lower right quadrant, closer to that of the observation and the truth.

Referring to Fig. 11, data assimilation without blending (EnDA, orange lines in Fig. 11) leads to a jump in the RMSE in the thermodynamic P variable upon the first assimilation at

$t = 25$ s. After that, the error stays relatively constant. The scale analysis in appendix C corroborates that the magnitude of this error jump is compatible with a spontaneous acoustic imbalance introduced by the data assimilation procedure.

Assimilating the momentum fields alone is insufficient and the RMSE in the solution (solid lines in Fig. 11) is larger than in the reference EnNoDA run. As expected, EnDAB provides a smoother solution over time as the error does not oscillate. This test includes a strong axisymmetric potential temperature variation (Fig. 4), and the potential temperature is an advected quantity not corrected by momentum data assimilation. Therefore, the initially tight correlation of the velocity and potential temperature variations gets destroyed in the course of data assimilation. Since the potential temperature is fluid dynamically active through the generation of baroclinic torque, the flow fields of the ensemble members increasingly deviate from their reference as a consequence.

Assimilating all the quantities yields an improvement (dashed lines in Fig. 11). While the initial assimilation reduces the error substantially for $\rho, \rho u$ and ρw of the EnDA run, the error increases over time until approximately $t = 150$ s. The increase in the error is due to the imbalances introduced by the chosen (11×11) grid point size of the localization regions [more details are provided in section 5c(3) and appendix C]. For the EnDAB run, the imbalances are suppressed and the RMSEs are lower than those of the control EnNoDA run for all quantities over the entire simulation period. Ensemble spread and RMSE are comparable in these traveling vortex runs (not shown).

2) RISING BUBBLE

Figure 12 displays snapshots of pressure perturbation for the bubble case. In the EnNoDA run (first row) the bubbles in the ensemble attain different heights at the end of the simulation time and the ensemble mean is diffused, in line with the spread in the initial conditions used in generating the ensemble. Ensemble members with larger initial potential temperature perturbation rise faster. In the EnDA ensemble (second row), large-amplitude fast-mode imbalances are present, while the ensemble mean of the bubble rotor positions at the end time better approximates the true positions of the rotors. For EnDAB (third row), the individual ensemble members are close to one another, as reflected in the ensemble mean. The ensemble better approximates the truth and the fast-mode imbalances are suppressed. Moreover, the pressure footprints of the bubble rotors are not visible in plots of the pressure differences between the EnDA and EnDAB ensembles (fourth row), showing that the difference between the EnDA and EnDAB results is predominantly due to the presence of the imbalances only, and suggesting (right column) that data assimilation is comparably effective in nudging the bubble toward the truth in both cases. Blending suppresses the imbalances while leaving the dynamics of the rising bubble largely unaffected.

RMSE plots of data assimilation of the momentum fields in the rising bubble experiment are shown in Fig. 13. The momentum fields are assimilated every 50.0 s after 500.0 s. This is visible in the momentum RMSE plots, where each downward step corresponds to one application of the assimilation procedure. For

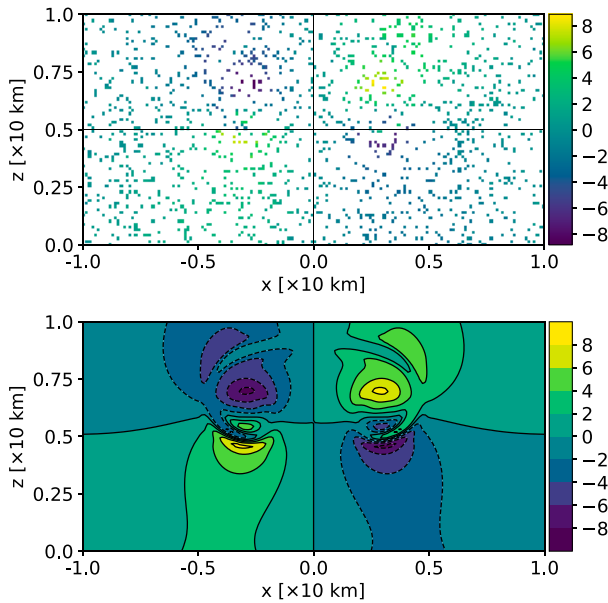


FIG. 9. Rising bubble: Horizontal momentum field ρu at $t = 1000.0$ s. (top) Sparse and noisy observations and (bottom) truth; contours in range $[-8, 8]$ $\text{kg m}^{-1} \text{s}^{-1}$ with a $2 \text{ kg m}^{-1} \text{s}^{-1}$ interval, negative contours dashed.

EnDA, an error is introduced in the density ρ and mass-weighted potential temperature P . Blending negates this error and the EnDAB curves show a smooth profile, with RMSE lower than the control EnNoDA. As in the traveling vortex case, a jump is visible in the RMSE of P at the first assimilation time for EnDA, and this corresponds to the imbalances introduced. See appendix C on the scale analysis for more details. The ensemble spread and RMSE are again comparable in these runs (not shown).

3) LOCALIZATION REGION AND IMBALANCES

In this section, results of the EnDA and EnDAB ensembles are investigated for varying localization radii. Here the aim is not to obtain the optimal choice of the localization radius but

to illustrate its effect on the imbalances. All the quantities are assimilated for the traveling vortex test case, and localization regions of (5×5) , (11×11) , (21×21) , and (41×41) grid points are used in addition to a run without localization (EnNoLoc). Otherwise, the setup follows the parameters laid out in section 5a(1) and Table 2.

The balanced structure of the vortex could be preserved for the quantities ρ , ρu , and ρw in the EnDA case. For these EnDA quantities, the localization length scale plays an important role.

If the localization region is too small, fewer observations are involved in the update of the analysis grid point, and the effect of data assimilation becomes less severe. As a result, the nudging of the vortices in the ensemble toward the truth is more gradual (Fig. 14). The drop in the RMSE after the first assimilation time at $t = 25$ s for the run with a (5×5) localization region (magenta solid with square markers) is the least drastic, and the RMSEs continue to drop for the subsequent assimilation step. However, the small localization region also introduces severe imbalances that deteriorate the compact vortex structure.

If the localization region is moderately small, e.g., (11×11) (solid orange line with triangle markers in Fig. 14), sufficient observation points are assimilated and the effect of data assimilation becomes significant. At the same time, the localization region is small enough such that the imbalances introduced are sufficient to deteriorate the compact vortex structure. In such a case, we see a relatively significant increase in the RMSE over time as the combined detrimental effects from a severe initial nudging of the vortices in the ensemble toward the truth and from the imbalances introduced by the localization are the most pronounced.

On the other hand, if the localization region is sufficiently small, e.g., (5×5) , the imbalances introduced by the localization remain severe, but the gentler nudging of the vortices in the ensemble toward the truth better preserves the compact vortex structure, and we do not see a drastic increase in the RMSEs as with the (11×11) run.

TABLE 2. Assimilation-related experimental parameters. Here, K is the ensemble size, b is the ensemble inflation factor, t_{first} is the first assimilation time, Δt_{obs} is the observation interval, $\psi_{\text{assimilated}}$ is the set of quantities assimilated, $(N \times N)_{\text{local}}$ is the size of the local region, f_{local} is the type of localization function, η_{obs} is the observation noise, $\text{obs}_{\text{sparse}}$ is the sparsity of the observations, and N_{blending} is the number of initial time steps spent in the limit model regime. The π' choice is used in the initialization of N_{blending} , more details in section 4c.

Test case		Vortex	Bubble
Ensemble	K	10 members	
	b	1.0	
Observations	t_{first} (s)	25.0	500.0
	Δt_{obs} (s)	25.0	50.0
	$\psi_{\text{assimilated}}$	$\{\rho u, \rho w\}$ or $\{\rho, \rho u, \rho w, P, \pi'\}$	$\{\rho u, \rho w\}$
	$(N \times N)_{\text{local}}$	(11×11) grid points	
	f_{local}	Truncated Gaussian	
Blending	η_{obs}	Gaussian with zero mean and variance in Table D1	
	$\text{obs}_{\text{sparse}}$	One in 10 grid points	
	N_{blending}	A single blended time step	
	π' choice	π'_{half}	

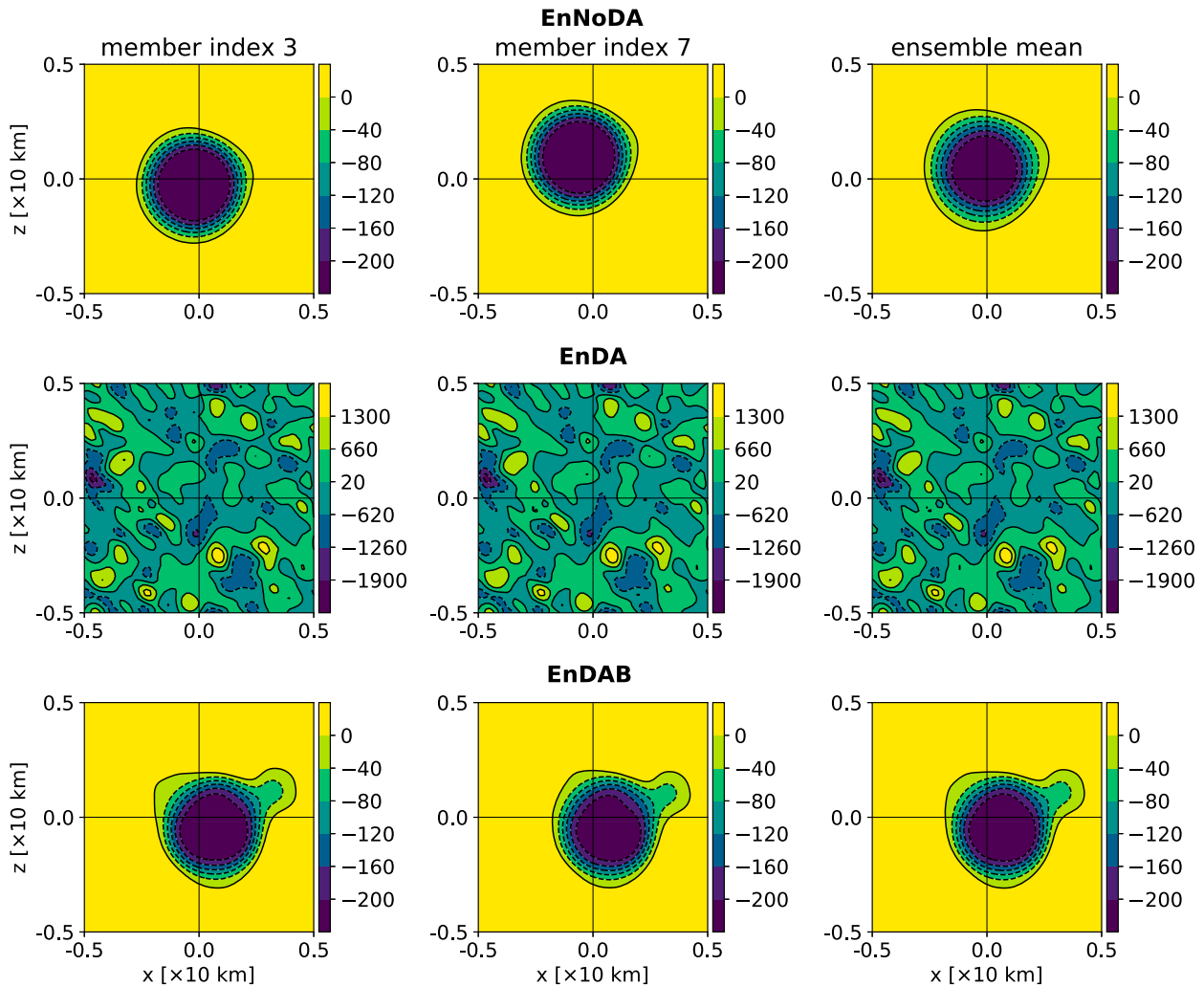


FIG. 10. Traveling vortex: Snapshots of pressure perturbation p' . Ensemble members with (left) index 3, (center) index 7, and (right) ensemble mean at $t = 300.0$ s with all quantities $\{\rho, \rho u, \rho v, P, \pi'\}$ assimilated. (top) EnNoDA run; contours in range $[-200, 0]$ Pa with a 40-Pa interval. (middle) EnDA run; contours in range $[-1900, 1300]$ Pa with a 640-Pa interval. (bottom) EnDAB run; contours in range $[-200, 0]$ Pa with a 40-Pa interval. Negative contours are dashed.

For larger localization regions, the imbalance introduced by local data assimilation is mitigated. In Fig. 14, the RMSE of EnDA runs with larger localization regions, e.g., (21×21) (yellow solid line with diamond markers) and (41×41) (cyan solid line with star markers) generally perform better than the other runs. We also note that a larger localization region corresponds to a smaller error jump in the variable P (top-right panel of Fig. 14). For the case without localization (EnNoLoc, solid brown line with cross markers), the error jump is almost nonexistent, but an imbalance is nevertheless introduced, see the fluctuation of the errors around that of the EnNoDA run (black solid dotted line).

A localization region that is too large leads to an erroneous oversampling of the dynamics. For example, the analysis update of grid points inside of the vortex structure is influenced by observations of the background dynamics and vice versa. This mutual

influence results in a vortex structure that becomes increasingly spread out as the number of assimilation steps increases. The effect of oversampling can be seen in, e.g., the EnNoLoc run in Fig. 14 and in the (41×41) and the EnNoLoc runs in Fig. 15, where the error scores are higher than in a run with a moderate localization region.

Application of blended data assimilation as a balancing mechanism eliminates the imbalances from a local data assimilation procedure. As a result, smaller localization regions may be used with fewer adverse effects, and the best error scores are achieved by an EnDAB run with a localization region of (11×11) grid points (dashed orange line with triangle markers in Fig. 15). The higher RMSE in the (5×5) run (dashed magenta line with square markers) may be due to the undersampling of the vortex dynamics. This is the opposite of the oversampling effect described above.

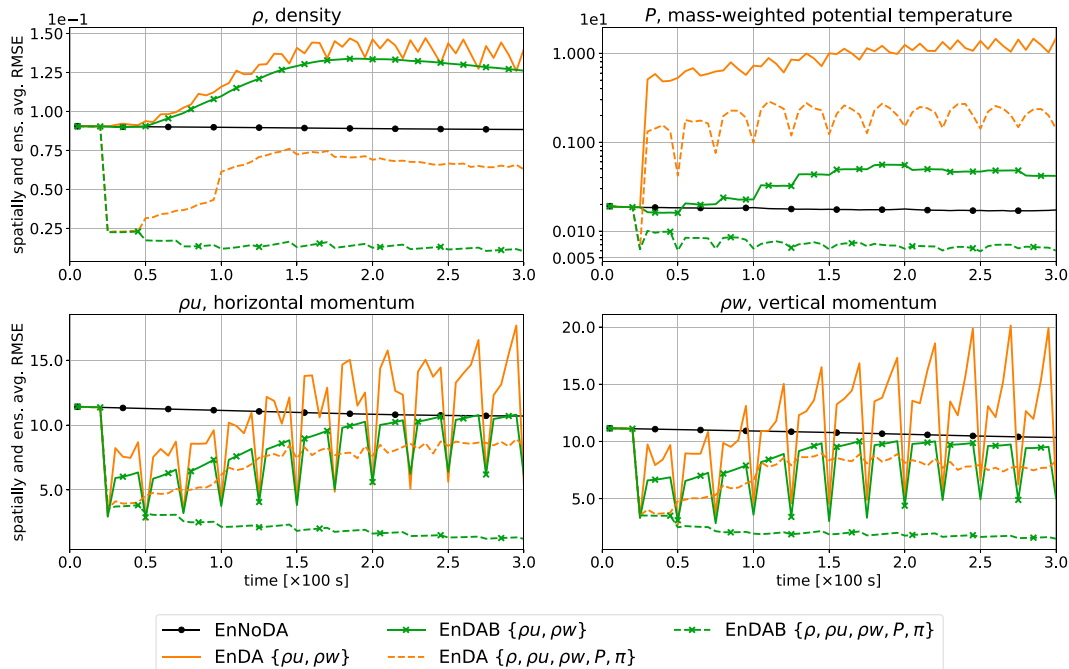


FIG. 11. Traveling vortex: EnNoDA run (solid dotted, black), EnDA run (orange), and EnDAB run (crossed green). Assimilated quantities are ρu and ρw (solid lines) and ρ , ρu , ρw , P , π' (dashed lines). Spatially and ensemble averaged RMSE from $t = 0.0$ to 300.0 s for (top left) density ρ (kg m^{-3}), (top right) mass-weighted potential temperature P (log-linear scale; $\text{kg m}^{-2} \text{K}$), and (bottom left) momentum ρu and (bottom right) momentum ρw ($\text{kg m}^{-1} \text{s}^{-1}$). The RMSE of the initial ensemble is omitted.

For the rising bubble experiments (results not shown), runs with assimilation of only the momentum fields and localization region sizes up to (71×71) grid points were investigated. For the quantities ρ , ρu and ρw , the RMSEs generally decrease with larger localization regions, although the decrease in the error is only marginal for localization region sizes larger than (41×41) grid points. As in the traveling vortex tests, for smaller localization regions, substantial error jumps in the P and π' variables are observed in the EnDA runs but not in the EnDAB runs.

6. Discussion and conclusions

This paper has presented a new conceptual framework for balanced data assimilation based on blended numerical models. Using a discrete time-level numerical analysis for the Exner pressure field and a careful choice of pressure perturbation variables, the blended soundproof-compressible modeling framework of Benacchio et al. (2014) has been substantially upgraded by a functionality to switch between equation sets in a single time step.

In idealized numerical experiments with a traveling vortex and a gravity-driven warm air bubble, a single time step in the pseudo-incompressible limit regime was sufficient to recover a balanced state starting from imbalanced initial data. Moreover, the blended model yielded leftover acoustics with amplitude more than one order of magnitude smaller than the ones generated at the onset with the fully compressible model. The

amplitude reduction is a sizeable improvement over the scores of Benacchio et al. (2014) who, in addition, needed several time steps in a hybrid soundproof-compressible configuration with noninteger values of the blending parameter α_P to achieve their best level of noise reduction.

The upgraded blended model has then been combined with a data assimilation engine and deployed as a tool to reduce imbalances introduced by regular assimilation of data within model runs. Numerical results on ensemble data assimilation with and without blending showed that while data assimilation alone produced imbalances that effectively destroyed important qualitative features of the solution in one of the test cases, data assimilation together with blending strongly reduced those imbalances and led to recovery of accurate results. Moreover, blended data assimilation was effective despite the untuned data assimilation parameters used in the investigations. Throughout our study, a single time step spent in the pseudo-incompressible limit regime after the assimilation of data was sufficient to restore a nearly balanced state, as documented by strongly reduced RMSEs with the blended model. The RMSEs of the blended data assimilation run are almost as low as the error scores obtained from assimilating data into a pseudo-incompressible ensemble run (results not shown).

For ensemble data assimilation experiments with the traveling vortex, assimilation of the momentum fields alone was found to be insufficient in the case of large variation of the potential temperature in the vortex core. In the course of

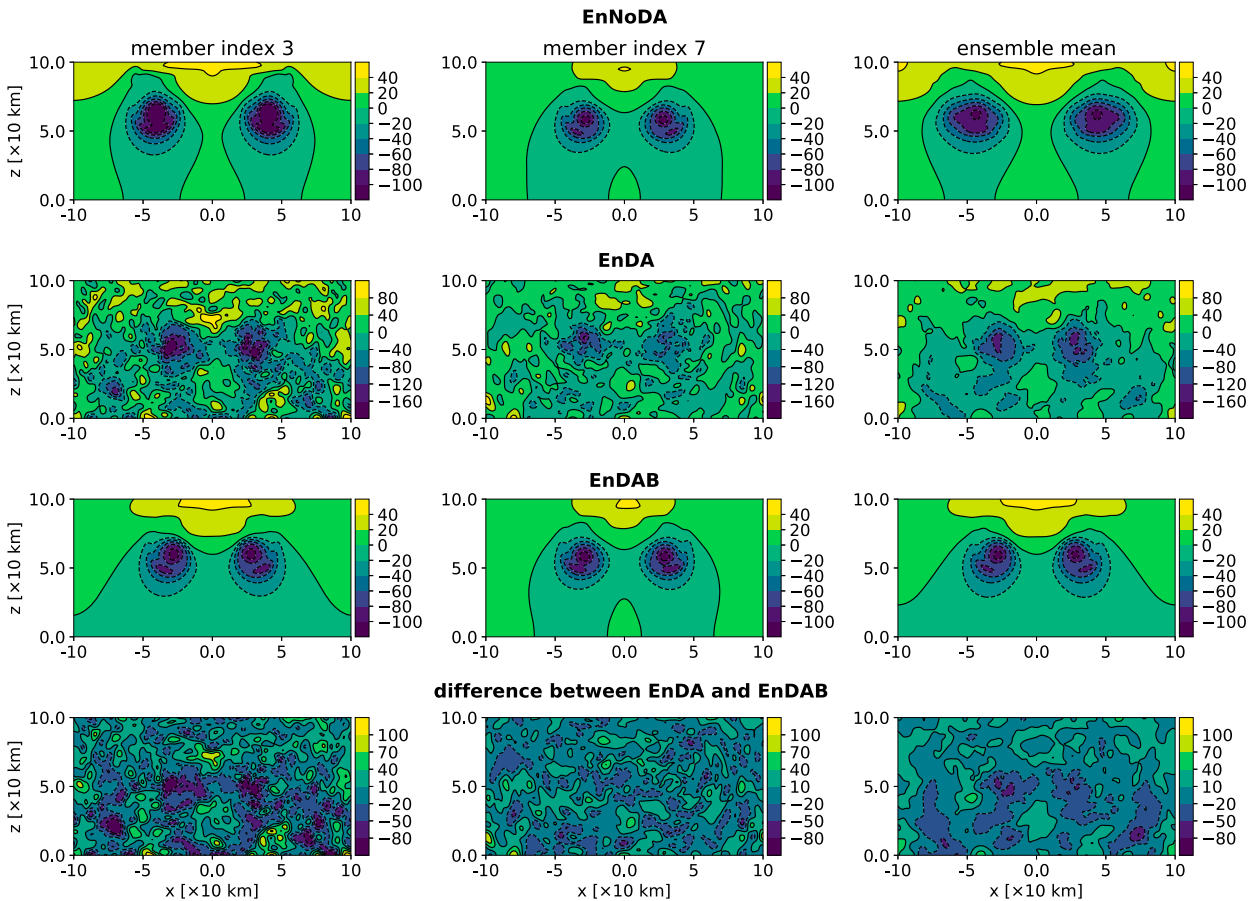


FIG. 12. Rising bubble: Snapshots of pressure perturbation p' . Ensemble members with (left) index 3 and (center) index 7 at $t = 1000.0$ s with (right) the ensemble mean. Shown from top to bottom are the EnNoDA run, contours in range $[-100, 40]$ Pa with a 20-Pa interval; EnDA run, contours in range $[-160, 80]$ Pa with a 40-Pa interval; EnDAB run, contours in range $[-100, 40]$ Pa with a 20-Pa interval; and difference between EnDA and EnDAB, contours in range $[-80, 100]$ Pa with a 30-Pa interval. Negative contours are dashed.

longer simulations, the ensemble with balanced data assimilation carried larger errors than the control ensemble without data assimilation with such a setup (green solid curves in Fig. 11). We associate this behavior with an issue of controllability (Jazwinski 2007): The potential temperature variations in this case are dynamically relevant owing to the generation of vorticity by baroclinic torque. Thus, if these variations are not assimilated, then the data assimilation steps will destroy the alignment of the pressure and density gradients in the vortex, and forecast quality will soon deteriorate. In fact, a test based on an analogous vortex with initially constant entropy yields results (not shown) close in quality to those of the rising thermal test when only momentum is assimilated. The issue was solved by assimilation of all variables. Further investigation is warranted on how the effectiveness of data assimilation can be improved under such circumstances without the need to observe all state variables.

A scale analysis (appendix C) corroborates the insight that the RMSE increase introduced by the assimilation of data corresponds to the fast-mode imbalances seen in the plots of

the individual ensemble members and the ensemble mean. In this sense, our experiments make a case for investigations involving relatively simple idealized test cases, as we were able to gain some analytical understanding of the sources and consequences of errors and imbalances. Nevertheless, further studies based on more realistic scenarios will be required to demonstrate that the presented approach and its extensions will actually enable quantifiable improvements of numerical weather prediction skill scores.

In the experiments involving ensemble data assimilation with different localization radii, blended data assimilation yielded, for all localization sizes, substantial improvements to the RMSE relative to the plain data assimilation without a balancing procedure. In fact, the best-performing data assimilation-only run still produced worse results than the worst-performing run with blending. Furthermore, the recovery of a balanced vortex structure turned out to be sensitive to the choice of localization radius, with best results obtained at some intermediate size of the localization domains. This study hints at a subtle interplay between the data assimilation setup and the idealized tests investigated in this paper, and further

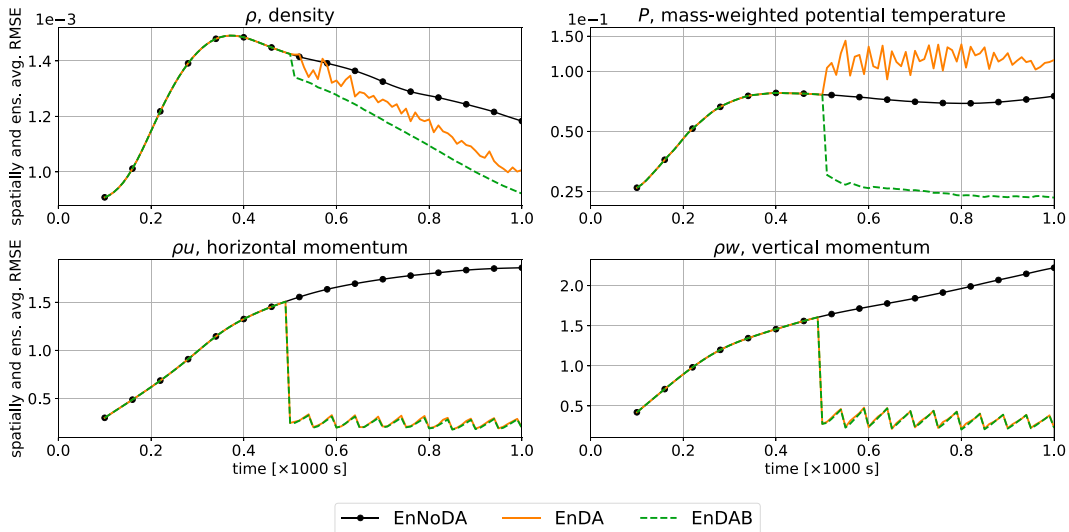


FIG. 13. Rising bubble: EnNoDA run (solid dotted, black), EnDA run (solid orange), EnDAB run (dashed green). Assimilated quantities are ρu and ρw . Spatially and ensemble averaged RMSE from $t = 100.0$ to 1000.0 s for (top left) density ρ (kg m^{-2}), (top right) mass-weighted potential temperature P (log-linear scale; $\text{kg m}^{-2} \text{K}$), and (bottom left) momentum ρu and (bottom right) momentum ρw ($\text{kg m}^{-1} \text{s}^{-1}$).

investigations into the effects of data assimilation on idealized and realistic dynamics are warranted.

In numerical weather prediction, methods to damp or remove acoustic imbalances have long been employed (e.g., Daley 1988; Skamarock and Klemp 1992; Dudhia 1995; Klemp et al. 2018). Moreover, practical application of sequential data assimilation procedures will generally excite all rapidly oscillatory modes of the compressible system,

and filtering techniques are used to negate these unphysical imbalances (Ha et al. 2017). In this context, the results presented in this paper are encouraging in that blended data assimilation was able to suppress acoustic noise and recover balanced analysis fields, albeit for idealized test cases. To the best of the authors' knowledge, this is the first study of a dynamics-driven method to suppress acoustic noise arising from the sequential assimilation of data.

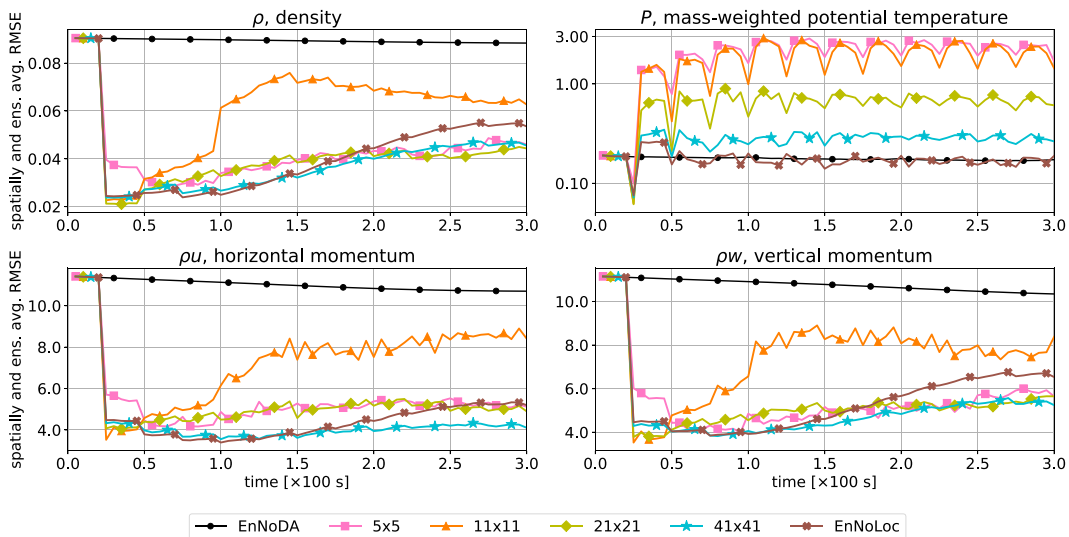


FIG. 14. Traveling vortex: EnNoDA (black dots) and EnDA experiments corresponding to localization regions with (5×5) (magenta squares), (11×11) (orange triangles), (21×21) (yellow diamonds), and (41×41) (cyan stars) grid points, and EnNoLoc without localization (brown crosses). Assimilated quantities are ρ , ρu , ρw , P , and π' . Spatially and ensemble averaged RMSE from $t = 0.0$ to 300.0 s for (top left) density ρ (kg m^{-2}), (top right) mass-weighted potential temperature P (log-linear scale; $\text{kg m}^{-2} \text{K}$), and (bottom left) momentum ρu and (bottom right) momentum ρw ($\text{kg m}^{-1} \text{s}^{-1}$). The RMSE of the initial ensemble is omitted.

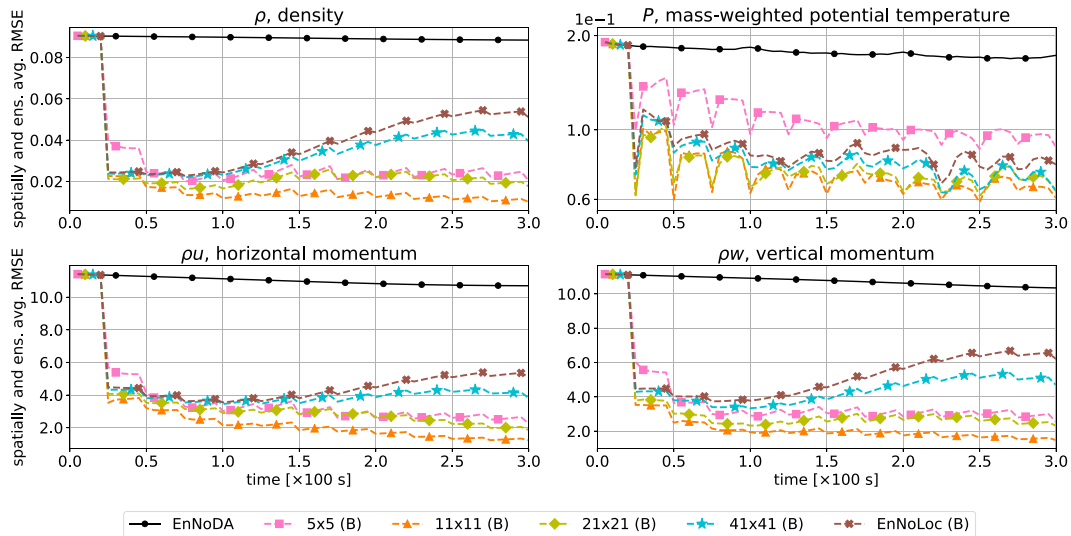


FIG. 15. Traveling vortex: EnNoDA (black dots) and EnDAB experiments corresponding to localization regions with (5×5) (magenta squares), (11×11) (orange triangles), (21×21) (yellow diamonds), and (41×41) (cyan stars) grid points, and EnNoLoc without localization (brown crosses). See Fig. 14 for the details of the panels.

In addition, the results presented in this paper prepare the ground for future work in a number of areas. In general, the performance of a data assimilation method can be improved by tuning its adjustable parameters. Here, however, we consciously employed an untuned data assimilation scheme known to produce unphysical imbalances to test the efficacy of our dynamics-driven method in removing them. Consequently, a comprehensive study similar to Popov and Sandu (2019) on multivariate tuning of the LETKF and localization parameters for the blended numerical model will be an avenue for future improvements of our approach. The study could also compare our method with existing balancing strategies, e.g., the IAU and the DFI, following Polavarapu et al. (2004). To ensure a fair comparison, optimizations of the IAU along the lines of Lei and Whitaker (2016) and He et al. (2020) may have to be carried out. A comparison of the effects of our dynamics-driven method on the slower dynamics against those of the DFI and IAU, which act as low-pass filters (Houtekamer and Zhang 2016; Polavarapu et al. 2004), will be particularly insightful.

Despite the untuned data assimilation scheme used, the blended model has given promising results, although thus far only for idealized test cases. Another natural evolution will hence involve model performance on more realistic three-dimensional moist dynamics scenarios with bottom topography (O’Neill and Klein 2014; Duarte et al. 2015) and on benchmarks at larger scales (Skamarock and Klemp 1994; Benacchio and Klein 2019).

Although presented and refined here for the blending between the compressible Euler equations and the pseudo-incompressible model only, the methodology translates to other scenarios as long as one can formulate the according projection onto appropriate reduced dynamics via implicit substeps of a semi or fully implicit scheme. Models imposing a divergence

constraint on the weighted velocity field as well as frameworks blending between nonhydrostatic and hydrostatic dynamics will naturally fit into the present approach.

Specifically, the numerical scheme proposed by Benacchio and Klein (2019) enables solution of the hydrostatic system in the large-scale limit in addition to the small-scale low Mach number limit considered in this paper. Therefore, a blended data assimilation framework such as the one presented here could be enhanced with hydrostatic blending and used in a two-way blended pseudo-incompressible/hydrostatic/compressible model (Klein and Benacchio 2016) exploiting the different dynamics in the equation sets.

Moreover, the theoretical framework developed in that paper also included the unified model by Arakawa and Konor (2009) as one of the reduced models. Thus, after an appropriate extension of the present numerical scheme, yet another framework for blended data assimilation can be developed. In fact, a variant of the fully compressible/Arakawa–Konor model pair has recently been presented by Qaddouri et al. (2021), and a related blending approach will allow for the filtering of smaller-scale acoustic noise while leaving the Lamb wave components dynamically unaffected. Investigations similar to the ones in this paper can then be made on balancing initial states and data assimilation for small- to planetary-scale dynamics using the resulting doubly blended model framework. Internal waves play an important role for atmospheric dynamics and they should not be removed indiscriminately after a data assimilation step. Therefore, the identification and removal of unwanted internal wave noise while keeping the physically meaningful wave spectrum is an additional challenge that will require further theoretical developments beyond the scope of this paper.

More generally, semi-implicit compressible models feature in several dynamical cores used by weather centers worldwide.

Notable examples include the currently operational hydrostatic IFS spectral transform model in use at the European Centre for Medium-Range Weather Forecasts (ECMWF; Wedi et al. 2013), and the Met Office's Unified Model (Davies et al. 2005; Wood et al. 2014), which has a hydrostatic-nonhydrostatic switch. ECMWF's next-generation nonhydrostatic compressible dynamical core, IFS-FVM (Kühnlein et al. 2019), actually uses a numerical discretization akin to the one considered in this paper and would therefore be an ideal candidate for a first implementation of the blended tools in a semioperational model. In addition, our approach will bear particular relevance to fully compressible operational models featuring the option of selectively employing the dynamics of a limit model (Wood et al. 2014; Melvin et al. 2019; Voitov et al. 2019; Qaddouri et al. 2021).

In this context, multimodel numerics with seamless switching could contribute to creating a level playing field to evaluate accuracy and performance with different equation sets in the same dynamical core. The positive evidence provided here in balancing data assimilation shows, in the authors' view, a considerable potential and potential impact of deploying the blended model framework across the whole forecast model chain.

Acknowledgments. R.C., G.H., and R.K. thank the Deutsche Forschungsgemeinschaft for the funding through the Collaborative Research Center (CRC) 1114 "Scaling cascades in complex systems," Project 235221301, Project A02: "Multiscale data and asymptotic model assimilation for atmospheric flows." T.B. was supported by the ESCAPE-2 project, European Union's Horizon 2020 research and innovation program (Grant 800897). We thank Sebastian Reich (U Potsdam) for the meaningful discussions on modeling the observation error covariance.

Data availability statement. The results reported in the paper can be generated using Python scripts linked to the Python source code hosted in the Freie Universität Berlin (FUB)'s GitLab page: https://git.imp.fu-berlin.de/raychew/RKLM_Reference. Currently, access to the repository is limited to users with an FUB account due to privacy concerns and can be granted on a case-by-case basis by contacting the corresponding author at ray.chew@fu-berlin.de.

APPENDIX A

LETKF Algorithm

The local ensemble transform Kalman filter (LETKF) algorithm presented here is a summary of the algorithm published by Hunt et al. (2007) in their paper, adapted to the blended numerical framework.

Start with an ensemble of K state vectors, $\{\mathbf{x}_{k,[g]}^f\} \in \mathbb{R}^{m_{[g]}}$ for $k = 1, \dots, K$. Furthermore, assume that a set of observations $\mathbf{y}_{\text{obs},[g]} \in \mathbb{R}^{l_{[g]}}$ with a known covariance $\mathbf{R}_{[g]} \in \mathbb{R}^{l_{[g]} \times l_{[g]}}$ is available. Here, m and l represent the dimension of the state and observation spaces, and the subscript $[g]$ represents the global state space, i.e., localization has not been applied.

- 1) Apply the forward operator \mathcal{H} to obtain the state vectors in the observation space:

$$\mathcal{H}\mathbf{x}_{k,[g]}^f = \mathbf{y}_{k,[g]}^f \in \mathbb{R}^{l_{[g]}}. \quad (\text{A1})$$

- 2) Stack the anomaly of the state and observation vectors to form the matrices:

$$\mathbf{X}_{[g]}^f = [\mathbf{x}_{1,[g]}^f - \bar{\mathbf{x}}_{[g]} | \dots | \mathbf{x}_{K,[g]}^f - \bar{\mathbf{x}}_{[g]}] \in \mathbb{R}^{m_{[g]} \times K}, \quad (\text{A2})$$

$$\mathbf{Y}_{[g]}^f = [\mathbf{y}_{1,[g]}^f - \bar{\mathbf{y}}_{[g]} | \dots | \mathbf{y}_{K,[g]}^f - \bar{\mathbf{y}}_{[g]}] \in \mathbb{R}^{l_{[g]} \times K}, \quad (\text{A3})$$

where $\bar{\mathbf{x}}_{[g]}$ ($\bar{\mathbf{y}}_{[g]}$) is the mean of the state vectors (in observation space) over the ensemble:

$$\bar{\mathbf{x}}_{[g]} = \frac{1}{K} \sum_{k=1}^K \mathbf{x}_{k,[g]}^f \in \mathbb{R}^{m_{[g]}}. \quad (\text{A4})$$

- 3) From $\mathbf{X}_{[g]}^f$ and $\mathbf{Y}_{[g]}^f$, select the local \mathbf{X}^f and \mathbf{Y}^f .
- 4) From the global observations $\mathbf{y}_{\text{obs},[g]}$ and observation covariance $\mathbf{R}_{[g]}$, select the corresponding local counterparts \mathbf{y}_{obs} and \mathbf{R} . Notice that the subscript $[g]$ is dropped when representing the local counterparts.
- 5) Solve the linear system $\mathbf{R}\mathbf{C}^T = \mathbf{Y}^f$ for $\mathbf{C} \in \mathbb{R}^{K \times l}$.
- 6) Optionally, apply a localization function to \mathbf{C} to modify the influence of the surrounding observations.
- 7) Compute the $K \times K$ gain matrix:

$$\mathbf{K} = \left[(K-1) \frac{1}{b} + \mathbf{C}\mathbf{Y}^f \right]^{-1}, \quad (\text{A5})$$

where $b \geq 1$ is the ensemble inflation factor.

- 8) Compute the $K \times K$ analysis weight matrix:
- $$\mathbf{W}^a = [(K-1) \mathbf{K}]^{1/2}. \quad (\text{A6})$$
- 9) Compute the K -dimension vector encoding the distance of the observations from the forecast ensemble:

$$\bar{\mathbf{w}}^a = \mathbf{K}(\mathbf{y}_{\text{obs}} - \bar{\mathbf{y}}^f), \quad (\text{A7})$$

and add $\bar{\mathbf{w}}^a$ to each column of \mathbf{W}^a to get a set of K weight vectors $\{\mathbf{w}_k^a\}$ with $k = 1, \dots, K$.

- 10) From the set of weight vectors, compute the analysis for each ensemble member:

$$\mathbf{x}_k^a = \mathbf{X}^f \mathbf{w}_k^a + \bar{\mathbf{x}}^f, \quad \text{for } k = 1, \dots, K. \quad (\text{A8})$$

- 11) Finally, recover the global analysis ensemble $\{\mathbf{x}_{k,[g]}^a\}$, $k = 1, \dots, K$.

This recovery depends on how the local regions were selected in (A2) and (A3). For local region surrounding the grid point under analysis, the reassembly of the global analysis ensemble is done by reassembling the analyzed grid points back into the global grid.

APPENDIX B

Initial Stable Vortex Configuration

The initial stable vortex configuration is given as follows. Specifically, for a vortex with radius R , the initial nondimensionalized density distribution is given by

$$\rho(x, z, t) = \begin{cases} 1 - \frac{1}{2}(1 - r^2)^6, & \text{if } r < R, \\ 1, & \text{otherwise,} \end{cases} \quad (\text{B1})$$

where r is the radial distance. The initial nondimensionalized pressure distribution is as follows:

$$p(x, z, t) = \begin{cases} p(r), & \text{if } r < R, \\ 0, & \text{otherwise,} \end{cases} \quad (\text{B2})$$

where

$$p(r) = -\frac{r^{36}}{72} + \frac{6r^{35}}{35} - \frac{15r^{34}}{17} + \frac{74r^{33}}{33} - \frac{57r^{32}}{32} - \frac{174r^{31}}{31} + \frac{269r^{30}}{15} - \frac{450r^{29}}{29} - \frac{153r^{28}}{8} + \frac{1564r^{27}}{27} - \frac{510r^{26}}{13} - \frac{204r^{25}}{5} + \frac{737r^{24}}{8} - \frac{1032r^{23}}{23} - \frac{477r^{22}}{11} + 64r^{21} - \frac{81r^{20}}{40} - \frac{1242r^{19}}{19} + \frac{731r^{18}}{9} - \frac{966r^{17}}{17} + \frac{219r^{16}}{8} - \frac{146r^{15}}{15} + \frac{18r^{14}}{7} - \frac{6r^{13}}{13} + \frac{r^{12}}{24}. \quad (\text{B3})$$

Otherwise, the rest of the initial vortex setup follows the setup in [Kadioglu et al. \(2008\)](#).

APPENDIX C

Scale Analysis for the Data Assimilation Error in the Pressure-Related Fields

[Figures 11 and 13](#) show that the assimilation of only the momentum fields leads to a jump in RMSE in the nonmomentum fields, and the assimilation of all quantities in [Fig. 11](#) leads to a jump in RMSE in the pressure-related P field. This increase in the error occurs after the first assimilation time and remains of the same order of magnitude for the duration of the simulation, quantifying the imbalance introduced by data assimilation. The imbalance can be characterized by a scale analysis ([Klein et al. 2001](#)).

The assimilation of the momentum fields leads to a change in the divergence of the velocity fields:

$$\nabla \cdot (\delta \mathbf{v}) = \frac{\partial \delta u}{\partial x} + \frac{\partial \delta w}{\partial z}, \quad (\text{C1})$$

where $(\delta u, \delta w)$ are the changes in the velocity fields due to the assimilation of momenta in the vertical slice experiments. Equation (C1) has the units per second (s^{-1}).

Observe from [Figs. 10 and 12](#) that the imbalance introduced by data assimilation are fast-mode acoustic waves. This effect is modeled as a wave oscillating with the peak amplitude right after the assimilation of data at the grid point under analysis. Therefore, for an oscillating wave

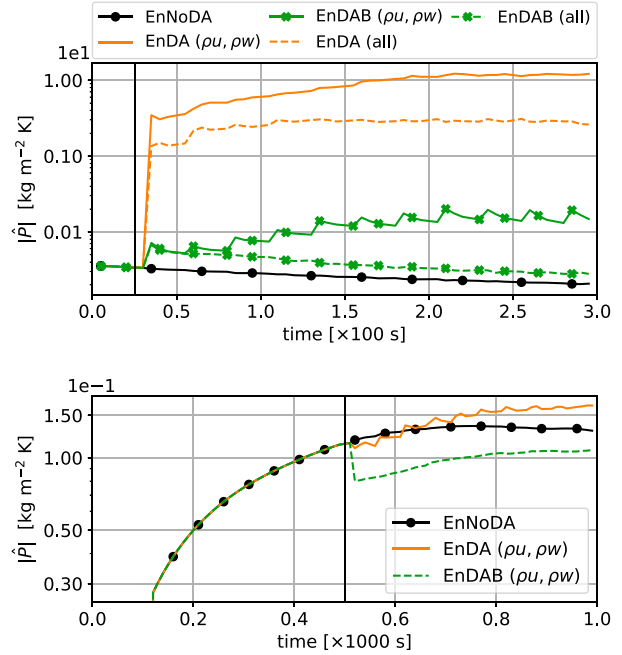


FIG. C1. Scale analysis of the contribution to the mass-weighted potential temperature P from the divergence of the velocity fields for (top) the traveling vortex ensemble and (bottom) the rising bubble ensemble. A semilogarithmic scale is used here. In the legend, (all) represents the traveling vortex ensembles with all quantities, $\{\rho, \rho_u, \rho_w, P, \pi'\}$, assimilated. The first assimilation time is marked with a vertical solid black line.

excited at grid point (x_i, z_j) , the maximum amplitude of the imbalances is

$$\begin{aligned} (\nabla \cdot \delta \mathbf{v})_{(i,j)} \int_0^{t_{ac}} \cos\left(\frac{\pi}{2} \frac{t}{t_{ac}}\right) dt &= \frac{2t_{ac}}{\pi} (\nabla \cdot \delta \mathbf{v})_{(i,j)} \left[\int_0^{\pi/2} \cos(\xi) d\xi \right] \\ &= \frac{2t_{ac}}{\pi} (\nabla \cdot \delta \mathbf{v})_{(i,j)}. \end{aligned} \quad (\text{C2})$$

The acoustic time scale t_{ac} is chosen as the time scale of the largest perturbations introduced. This is the time a wave takes to traverse to the edge of the (11×11) grid points local region from the analysis grid point. Therefore,

$$t_{ac} = \frac{11}{2} \frac{dx}{c_{ref}}, \quad (\text{C3})$$

where dx is the constant grid size and c_{ref} the speed of sound. Equation (C3) has units of seconds and (C2) is dimensionless.

As $p = \rho c_{ref}^2$, the contribution to the pressure from $\nabla \cdot (\delta \mathbf{v})_{(i,j)}$ is computed by

$$\frac{2t_{ac}}{\pi} \nabla \cdot (\delta \mathbf{v})_{(i,j)} \rho_{(i,j)} c_{ref}^2 \sim \hat{P}_{(i,j)}, \quad (\text{C4})$$

which has the units of pascals. The hat $\hat{\cdot}$ signifies that the quantity is obtained from scale analysis. Finally, use the equation of state (6) to obtain an estimate for \hat{P} .

TABLE D1. Values of the error variance in the observations of the traveling vortex and rising bubble test cases, computed as 5% of the variance of the sparsely observed fields averaged over all observation time.

Quantity	Variance	
	Vortex	Bubble
Density (ρ)	$4.5 \times 10^{-4} \text{ kg m}^{-2}$	—
Horizontal momentum (ρu)	$0.064 \text{ kg m}^{-1} \text{ s}^{-1}$	$0.022 \text{ kg m}^{-1} \text{ s}^{-1}$
Vertical momentum (ρw)	$0.064 \text{ kg m}^{-1} \text{ s}^{-1}$	$0.032 \text{ kg m}^{-1} \text{ s}^{-1}$
Mass-weighted potential temperature (P)	$6.7 \times 10^{-6} \text{ kg m}^{-2} \text{ K}$	—
Exner pressure perturbation (π')	2.4×10^{-7}	—

For comparison with the RMSE, the norm is taken for \hat{P} , given by

$$|\hat{P}| = \frac{1}{K} \sum_k \left[\sqrt{\frac{1}{N_x \times N_z} \sum_{ij}^{N_x, N_z} [\hat{P}_{(ij)}]^2} \right]_k, \quad (\text{C5})$$

where k indexes the K ensemble members and N_x and N_z are the number of grid points in the x and z coordinates.

Figure C1 shows the results of scale analysis for the two test cases. Results at assimilation time are omitted. Scale analysis yields EnDA results for $|\hat{P}|$ that are of the same order of magnitude as the jumps in the RMSE plots (Figs. 11 and 13) with a similar profile over time. The scale analysis in this appendix characterizes the error jump in the thermodynamical RMSE plots as fast-mode imbalances introduced through data assimilation.

APPENDIX D

Modeling the Observational Noise

The observational noise used in the data assimilation experiments is drawn from a Gaussian distribution. This Gaussian distribution has zero mean and a variance that is approximately 5% of the variance of the sparsely observed field averaged over all observation time. Specifically, the variances given in Table D1 are computed as follows.

For a sparsely observed quantity without measurement noise $\mathcal{Y}_{\text{obs}}^n$ at observation time t_{obs}^n , compute the variance:

$$(\sigma_{\text{y}_{\text{obs}}}^n)^2 = \frac{1}{N_{\text{obs}}} \sum_s^{N_{\text{obs}}} [\mathcal{Y}_{\text{obs}}^n(x, z)_s - \overline{\mathcal{Y}_{\text{obs}}^n}]^2, \quad (\text{D1})$$

where s indexes the number of sparse observations N_{obs} , and $(x, z)_s$ represents the (x, z) spatial point for the s th sparse observation. The term $\overline{\mathcal{Y}_{\text{obs}}^n}$ is the mean of the sparsely observed field $\mathcal{Y}_{\text{obs}}^n$ at observation time t_{obs}^n :

$$\overline{\mathcal{Y}_{\text{obs}}^n} = \frac{1}{N_{\text{obs}}} \sum_s^{N_{\text{obs}}} \mathcal{Y}_{\text{obs}}^n(x, z)_s. \quad (\text{D2})$$

This gives us the variance $(\sigma_{\text{y}_{\text{obs}}}^n)^2$ for each sparsely observed quantity at each observation time $\{t_{\text{obs}}^1, t_{\text{obs}}^2, \dots, t_{\text{obs}}^N\}$. Finally, the time-average of 5% of the variance for each of the observed quantities is taken:

$$\overline{\sigma_{\text{y}_{\text{obs}}}^2} = \frac{1}{N} \sum_n^N 0.05 (\sigma_{\text{y}_{\text{obs}}}^n)^2. \quad (\text{D3})$$

REFERENCES

- Anderson, J. L., 2007: An adaptive covariance inflation error correction algorithm for ensemble filters. *Tellus*, **59**, 210–224, <https://doi.org/10.1111/j.1600-0870.2006.00216.x>.
- Arakawa, A., and C. S. Konor, 2009: Unification of the anelastic and quasi-hydrostatic systems of equations. *Mon. Wea. Rev.*, **137**, 710–726, <https://doi.org/10.1175/2008MWR2520.1>.
- Bannister, R. N., 2015: How is the balance of a forecast ensemble affected by adaptive and nonadaptive localization schemes? *Mon. Wea. Rev.*, **143**, 3680–3699, <https://doi.org/10.1175/MWR-D-14-00379.1>.
- Benacchio, T., and R. Klein, 2019: A semi-implicit compressible model for atmospheric flows with seamless access to soundproof and hydrostatic dynamics. *Mon. Wea. Rev.*, **147**, 4221–4240, <https://doi.org/10.1175/MWR-D-19-0073.1>.
- , W. P. O'Neill, and R. Klein, 2014: A blended soundproof-to-compressible numerical model for small-to mesoscale atmospheric dynamics. *Mon. Wea. Rev.*, **142**, 4416–4438, <https://doi.org/10.1175/MWR-D-13-00384.1>.
- Bloom, S., L. Takacs, A. Da Silva, and D. Ledvina, 1996: Data assimilation using incremental analysis updates. *Mon. Wea. Rev.*, **124**, 1256–1271, [https://doi.org/10.1175/1520-0493\(1996\)124<1256:DAUIAU>2.0.CO;2](https://doi.org/10.1175/1520-0493(1996)124<1256:DAUIAU>2.0.CO;2).
- Bocquet, M., 2011: Ensemble Kalman filtering without the intrinsic need for inflation. *Nonlinear Processes Geophys.*, **18**, 735–750, <https://doi.org/10.5194/npg-18-735-2011>.
- Cohn, S. E., A. Da Silva, J. Guo, M. Sienkiewicz, and D. Lamich, 1998: Assessing the effects of data selection with the DAO physical-space statistical analysis system. *Mon. Wea. Rev.*, **126**, 2913–2926, [https://doi.org/10.1175/1520-0493\(1998\)126<2913:ATEODS>2.0.CO;2](https://doi.org/10.1175/1520-0493(1998)126<2913:ATEODS>2.0.CO;2).
- Daley, R., 1988: The normal modes of the spherical non-hydrostatic equations with applications to the filtering of acoustic modes. *Tellus*, **40**, 96–106, <https://doi.org/10.3402/tellusa.v40i2.11785>.
- Davies, T., M. J. P. Cullen, A. J. Malcolm, M. Mawson, A. Staniforth, A. A. White, and N. Wood, 2005: A new dynamical core for the Met Office's global and regional modelling of the atmosphere. *Quart. J. Roy. Meteor. Soc.*, **131**, 1759–1782, <https://doi.org/10.1256/qj.04.101>.
- Duarte, M., A. S. Almgren, and J. B. Bell, 2015: A low Mach number model for moist atmospheric flows. *J. Atmos. Sci.*, **72**, 1605–1620, <https://doi.org/10.1175/JAS-D-14-0248.1>.

- Dudhia, J., 1995: Reply to comments on “A nonhydrostatic version of the Penn State–NCAR mesoscale model: Validation tests and simulation of an Atlantic cyclone and cold front.” *Mon. Wea. Rev.*, **123**, 2573–2575, [https://doi.org/10.1175/1520-0493\(1995\)123<2573:R>2.0.CO;2](https://doi.org/10.1175/1520-0493(1995)123<2573:R>2.0.CO;2).
- Durran, D. R., 1989: Improving the anelastic approximation. *J. Atmos. Sci.*, **46**, 1453–1461, [https://doi.org/10.1175/1520-0469\(1989\)046<1453:ITAA>2.0.CO;2](https://doi.org/10.1175/1520-0469(1989)046<1453:ITAA>2.0.CO;2).
- Fisher, R. A., and F. Yates, 1953: *Statistical Tables for Biological, Agricultural and Medical Research*. 3rd ed. Hafner Publishing Company, 112 pp.
- Flowerdew, J., 2015: Towards a theory of optimal localisation. *Tellus*, **67A**, 25257, <https://doi.org/10.3402/tellusa.v67.25257>.
- Fukumori, I., 2002: A partitioned Kalman filter and smoother. *Mon. Wea. Rev.*, **130**, 1370–1383, [https://doi.org/10.1175/1520-0493\(2002\)130<1370:APKFAS>2.0.CO;2](https://doi.org/10.1175/1520-0493(2002)130<1370:APKFAS>2.0.CO;2).
- Gaspari, G., and S. E. Cohn, 1999: Construction of correlation functions in two and three dimensions. *Quart. J. Roy. Meteor. Soc.*, **125**, 723–757, <https://doi.org/10.1002/qj.49712555417>.
- Greybush, S. J., E. Kalnay, T. Miyoshi, K. Ide, and B. R. Hunt, 2011: Balance and ensemble Kalman filter localization techniques. *Mon. Wea. Rev.*, **139**, 511–522, <https://doi.org/10.1175/2010MWR3328.1>.
- Ha, S., C. Snyder, W. C. Skamarock, J. Anderson, and N. Collins, 2017: Ensemble Kalman filter data assimilation for the Model for Prediction Across Scales (MPAS). *Mon. Wea. Rev.*, **145**, 4673–4692, <https://doi.org/10.1175/MWR-D-17-0145.1>.
- Hamill, T. M., J. S. Whitaker, and C. Snyder, 2001: Distance-dependent filtering of background error covariance estimates in an ensemble Kalman filter. *Mon. Wea. Rev.*, **129**, 2776–2790, [https://doi.org/10.1175/1520-0493\(2001\)129<2776:DDFOBE>2.0.CO;2](https://doi.org/10.1175/1520-0493(2001)129<2776:DDFOBE>2.0.CO;2).
- Harlim, J., and B. R. Hunt, 2005: Local ensemble transform Kalman filter: An efficient scheme for assimilating atmospheric data. University of Maryland, College Park, 18 pp., https://www2.atmos.umd.edu/~ekalnay/pubs/harlim_hunt05.pdf.
- Hastermann, G., M. Reinhardt, R. Klein, and S. Reich, 2021: Balanced data assimilation for highly oscillatory mechanical systems. *Commun. Appl. Math. Comput. Sci.*, **16**, 119–154, <https://doi.org/10.2140/camos.2021.16.119>.
- He, H., L. Lei, J. S. Whitaker, and Z.-M. Tan, 2020: Impacts of assimilation frequency on ensemble Kalman filter data assimilation and imbalances. *J. Adv. Model. Earth Syst.*, **12**, e2020MS002187, <https://doi.org/10.1029/2020MS002187>.
- Hohenegger, C., and C. Schär, 2007: Predictability and error growth dynamics in cloud-resolving models. *J. Atmos. Sci.*, **64**, 4467–4478, <https://doi.org/10.1175/2007JAS2143.1>.
- Houtekamer, P. L., and H. L. Mitchell, 1998: Data assimilation using an ensemble Kalman filter technique. *Mon. Wea. Rev.*, **126**, 796–811, [https://doi.org/10.1175/1520-0493\(1998\)126<0796:DAUAEK>2.0.CO;2](https://doi.org/10.1175/1520-0493(1998)126<0796:DAUAEK>2.0.CO;2).
- , and F. Zhang, 2016: Review of the ensemble Kalman filter for atmospheric data assimilation. *Mon. Wea. Rev.*, **144**, 4489–4532, <https://doi.org/10.1175/MWR-D-15-0440.1>.
- Hunt, B. R., E. J. Kostelich, and I. Szunyogh, 2007: Efficient data assimilation for spatiotemporal chaos: A local ensemble transform Kalman filter. *Physica D*, **230**, 112–126, <https://doi.org/10.1016/j.physd.2006.11.008>.
- Jazwinski, A. H., 2007: *Stochastic Processes and Filtering Theory*. Dover Publications, 376 pp.
- Kadioglu, S. Y., R. Klein, and M. L. Minion, 2008: A fourth-order auxiliary variable projection method for zero-Mach number gas dynamics. *J. Comput. Phys.*, **227**, 2012–2043, <https://doi.org/10.1016/j.jcp.2007.10.008>.
- Kalman, R. E., 1960: A new approach to linear filtering and prediction problems. *J. Basic Eng.*, **82**, 35–45, <https://doi.org/10.1115/1.3662552>.
- Keper, J. D., 2009: Covariance localisation and balance in an ensemble Kalman filter. *Quart. J. Roy. Meteor. Soc.*, **135**, 1157–1176, <https://doi.org/10.1002/qj.443>.
- Klein, R., 2009: Asymptotics, structure, and integration of sound-proof atmospheric flow equations. *Theor. Comput. Fluid Dyn.*, **23**, 161–195, <https://doi.org/10.1007/s00162-009-0104-y>.
- , 2010: Scale-dependent models for atmospheric flows. *Annu. Rev. Fluid Mech.*, **42**, 249–274, <https://doi.org/10.1146/annurev-fluid-121108-145537>.
- , and O. Pauluis, 2012: Thermodynamic consistency of a pseudo-incompressible approximation for general equations of state. *J. Atmos. Sci.*, **69**, 961–968, <https://doi.org/10.1175/JAS-D-11-0110.1>.
- , and T. Benacchio, 2016: A doubly blended model for multi-scale atmospheric dynamics. *J. Atmos. Sci.*, **73**, 1179–1186, <https://doi.org/10.1175/JAS-D-15-0323.1>.
- , N. Botta, T. Schneider, C.-D. Munz, S. Roller, A. Meister, L. Hoffmann, and T. Sonar, 2001: Asymptotic adaptive methods for multi-scale problems in fluid mechanics. *J. Eng. Math.*, **39**, 261–343, <https://doi.org/10.1023/A:1004844002437>.
- , U. Achatz, D. Bresch, O. M. Knio, and P. K. Smolarkiewicz, 2010: Regime of validity of sound-proof atmospheric flow models. *J. Atmos. Sci.*, **67**, 3226–3237, <https://doi.org/10.1175/2010JAS3490.1>.
- , T. Benacchio, and W. O’Neill, 2014: Using the sound-proof limit for balanced data initialization. *Proc. ECMWF Seminar on Numerical Methods*, ECMWF, Reading, United Kingdom, 227–236, <https://www.ecmwf.int/sites/default/files/elibrary/2014/10483-using-sound-proof-limit-balanced-data-initialization.pdf>.
- Klemp, J. B., W. C. Skamarock, and S. Ha, 2018: Damping acoustic modes in compressible horizontally explicit vertically implicit (HEVI) and split-explicit time integration schemes. *Mon. Wea. Rev.*, **146**, 1911–1923, <https://doi.org/10.1175/MWR-D-17-0384.1>.
- Kühnlein, C., W. Deconinck, R. Klein, S. Malardel, Z. P. Piotrowski, P. K. Smolarkiewicz, J. Szmelter, and N. P. Wedi, 2019: FVM 1.0: A nonhydrostatic finite-volume dynamical core for the IFS. *Geosci. Model Dev.*, **12**, 651–676, <https://doi.org/10.5194/gmd-12-651-2019>.
- Lang, M., P. Browne, P. J. Van Leeuwen, and M. Owens, 2017: Data assimilation in the solar wind: Challenges and first results. *Space Wea.*, **15**, 1490–1510, <https://doi.org/10.1002/2017SW001681>.
- Lei, L., and J. S. Whitaker, 2016: A four-dimensional incremental analysis update for the ensemble Kalman filter. *Mon. Wea. Rev.*, **144**, 2605–2621, <https://doi.org/10.1175/MWR-D-15-0246.1>.
- Lorenc, A. C., 2003: The potential of the ensemble Kalman filter for NWP—A comparison with 4D-Var. *Quart. J. Roy. Meteor. Soc.*, **129**, 3183–3203, <https://doi.org/10.1256/qj.02.132>.
- Lynch, P., and X.-Y. Huang, 1992: Initialization of the HIRLAM model using a digital filter. *Mon. Wea. Rev.*, **120**, 1019–1034, [https://doi.org/10.1175/1520-0493\(1992\)120<1019:IOTHMU>2.0.CO;2](https://doi.org/10.1175/1520-0493(1992)120<1019:IOTHMU>2.0.CO;2).
- Melvin, T., T. Benacchio, B. Shipway, N. Wood, J. Thuburn, and C. Cotter, 2019: A mixed finite-element, finite-volume, semi-implicit discretization for atmospheric dynamics: Cartesian

- geometry. *Quart. J. Roy. Meteor. Soc.*, **145**, 2835–2853, <https://doi.org/10.1002/qj.3501>.
- Mendez-Nunez, L. R., and J. J. Carroll, 1994: Application of the MacCormack scheme to atmospheric nonhydrostatic models. *Mon. Wea. Rev.*, **122**, 984–1000, [https://doi.org/10.1175/1520-0493\(1994\)122<0984:AOTMST>2.0.CO;2](https://doi.org/10.1175/1520-0493(1994)122<0984:AOTMST>2.0.CO;2).
- Mitchell, H. L., P. L. Houtekamer, and G. Pellerin, 2002: Ensemble size, balance, and model-error representation in an ensemble Kalman filter. *Mon. Wea. Rev.*, **130**, 2791–2808, [https://doi.org/10.1175/1520-0493\(2002\)130<2791:ESBAME>2.0.CO;2](https://doi.org/10.1175/1520-0493(2002)130<2791:ESBAME>2.0.CO;2).
- Neef, L. J., S. M. Polavarapu, and T. G. Shepherd, 2006: Four-dimensional data assimilation and balanced dynamics. *J. Atmos. Sci.*, **63**, 1840–1858, <https://doi.org/10.1175/JAS3714.1>.
- O'Neill, W., and R. Klein, 2014: A moist pseudo-incompressible model. *Atmos. Res.*, **142**, 133–141, <https://doi.org/10.1016/j.atmosres.2013.08.004>.
- Pedlosky, J., 2013: *Geophysical Fluid Dynamics*. 2nd ed. Springer, 710 pp.
- Polavarapu, S., S. Ren, A. M. Clayton, D. Sankey, and Y. Rochon, 2004: On the relationship between incremental analysis updating and incremental digital filtering. *Mon. Wea. Rev.*, **132**, 2495–2502, [https://doi.org/10.1175/1520-0493\(2004\)132<2495:OTRBIA>2.0.CO;2](https://doi.org/10.1175/1520-0493(2004)132<2495:OTRBIA>2.0.CO;2).
- Popov, A. A., and A. Sandu, 2019: A Bayesian approach to multivariate adaptive localization in ensemble-based data assimilation with time-dependent extensions. *Nonlinear Processes Geophys.*, **26**, 109–122, <https://doi.org/10.5194/npg-26-109-2019>.
- Qaddouri, A., C. Girard, S. Z. Husain, and R. Aider, 2021: Implementation of a semi-Lagrangian fully implicit time integration of the unified soundproof system of equations for numerical weather prediction. *Mon. Wea. Rev.*, **149**, 2011–2029, <https://doi.org/10.1175/MWR-D-20-0291.1>.
- Reich, S., and C. Cotter, 2013: Ensemble filter techniques for intermittent data assimilation. *Large Scale Inverse Problems: Computational Methods and Applications in the Earth Sciences*, S. K. M. Cullen, M. A. Freitag, and R. Scheichl, Eds., Radon Series on Computational and Applied Mathematics, Vol. 13, De Gruyter, 91–134.
- , and —, 2015: *Probabilistic Forecasting and Bayesian Data Assimilation*. Cambridge University Press, 308 pp.
- Skamarock, W. C., and J. B. Klemp, 1992: The stability of time-split numerical methods for the hydrostatic and the nonhydrostatic elastic equations. *Mon. Wea. Rev.*, **120**, 2109–2127, [https://doi.org/10.1175/1520-0493\(1992\)120<2109:TSOTSN>2.0.CO;2](https://doi.org/10.1175/1520-0493(1992)120<2109:TSOTSN>2.0.CO;2).
- , and —, 1994: Efficiency and accuracy of the Klemp–Wilhelmson time-splitting technique. *Mon. Wea. Rev.*, **122**, 2623–2630, [https://doi.org/10.1175/1520-0493\(1994\)122<2623:EAAOTK>2.0.CO;2](https://doi.org/10.1175/1520-0493(1994)122<2623:EAAOTK>2.0.CO;2).
- Smolarkiewicz, P. K., 1991: On forward-in-time differencing for fluids. *Mon. Wea. Rev.*, **119**, 2505–2510, [https://doi.org/10.1175/1520-0493\(1991\)119<2505:OFITDF>2.0.CO;2](https://doi.org/10.1175/1520-0493(1991)119<2505:OFITDF>2.0.CO;2).
- , and L. O. Margolin, 1993: On forward-in-time differencing for fluids: Extension to a curvilinear framework. *Mon. Wea. Rev.*, **121**, 1847–1859, [https://doi.org/10.1175/1520-0493\(1993\)121<1847:OFITDF>2.0.CO;2](https://doi.org/10.1175/1520-0493(1993)121<1847:OFITDF>2.0.CO;2).
- , and A. Dörnbrack, 2008: Conservative integrals of adiabatic Durran's equations. *Int. J. Numer. Methods Fluids*, **56**, 1513–1519, <https://doi.org/10.1002/flid.1601>.
- , C. Kühnlein, and N. P. Wedi, 2014: A consistent framework for discrete integrations of soundproof and compressible PDEs of atmospheric dynamics. *J. Comput. Phys.*, **263**, 185–205, <https://doi.org/10.1016/j.jcp.2014.01.031>.
- Vallis, G. K., 2017: *Atmospheric and Oceanic Fluid Dynamics: Fundamentals and Large-Scale Circulation*. 2nd ed. Cambridge University Press, 964 pp.
- Van Leeuwen, P. J., Y. Cheng, and S. Reich, 2015: *Nonlinear Data Assimilation*. Springer, 118 pp.
- Voitus, F., P. Bénard, C. Kühnlein, and N. P. Wedi, 2019: Semi-implicit integration of the unified equations in a mass-based coordinate: Model formulation and numerical testing. *Quart. J. Roy. Meteor. Soc.*, **145**, 3387–3408, <https://doi.org/10.1002/qj.3626>.
- Wedi, N. P., M. Hamrud, and G. Mozdzyński, 2013: A fast spherical harmonics transform for global NWP and climate models. *Mon. Wea. Rev.*, **141**, 3450–3461, <https://doi.org/10.1175/MWR-D-13-00016.1>.
- Wikle, C. K., and L. M. Berliner, 2007: A Bayesian tutorial for data assimilation. *Physica D*, **230**, 1–16, <https://doi.org/10.1016/j.physd.2006.09.017>.
- Wood, N., and Coauthors, 2014: An inherently mass-conserving semi-implicit semi-Lagrangian discretization of the deep-atmosphere global non-hydrostatic equations. *Quart. J. Roy. Meteor. Soc.*, **140**, 1505–1520, <https://doi.org/10.1002/qj.2235>.
- Zupanski, M., 2009: Theoretical and practical issues of ensemble data assimilation in weather and climate. *Data Assimilation for Atmospheric, Oceanic and Hydrologic Applications*, S. K. Park and L. Xu, Eds., Vol. 1, Springer, 67–84.